JOURNAL OF GEOPHYSICAL RESEARCH: OCEANS, VOL. 118, 3979–3998, doi:10.1002/jgrc.20289, 2013

Modulation of the sea-surface temperature in the Southeast Pacific by the atmospheric low-level coastal jet

Xiaodong Hong,[1] Shouping Wang,[1] Teddy R. Holt,[1] Paul J. Martin,[2] and Larry O'Neill[3]

Received 14 May 2012; revised 30 April 2013; accepted 25 June 2013; published 3 September 2013.

[1] The atmospheric low-level coastal jet (LLCJ) in the Southeast Pacific (SEP) region is characterized as either a strong-forcing jet (colder and drier air) or weak-forcing jet (warm and moist) based on the location of the Southeast Pacific high-pressure system (SEPH). The sea-surface temperature (SST) changes corresponding to a particularly strong-forcing jet (29–30 October) and weak-forcing jet (22–23 November) are investigated in this study using the two-way air-ocean coupled model COAMPS® and satellite observation data. Results indicate that the coupled simulation reduces the overall absolute bias 50% for the surface wind speed, 70% for the cloud liquid water path, and 15% for SST as compared to the uncoupled simulation. The coupled simulation reduces excessive SST cooling, especially during the strong-forcing jet period along the coastal area where offshore transport of upwelled cold water is too strong from the uncoupled simulation. The coupled simulation also reduces the excessive warming from the uncoupled simulation by providing better cloud coverage. The prominent mechanisms in cooling SST along the coast are the same for both the strong-forcing and weak-forcing jets, namely vigorous upwelling and horizontal advection. However, the mechanisms along the jet path differ from along the coast, with air-sea heat exchange the most important process, resulting in cooling SST during the strong-forcing jet period but warming SST during the weak-forcing jet period. The advances and differences of the present study as compared with previous studies are discussed in detail in the paper.

Citation: Hong, X., S. Wang, T. R. Holt, P. J. Martin, and L. O'Neill (2013), Modulation of the sea surface temperature in the Southeast Pacific by the atmospheric low-level coastal jet, *J. Geophys. Res. Oceans*, *118*, 3979–3998, doi:10.1002/jgrc.20289.

1. Introduction

[2] The low-level coastal jet off the central Chilean coast features an elongated maximum of surface wind speed exceeding 10 ms^{-1} as seen from Quick Scatterometer (QuikSCAT) observations [*Muñoz and Garreaud*, 2005]. The jet axis is located approximately 150 km from the coastline and has a cross-shore scale of about 500 km. The LLCJ events occur most frequently during spring and summer (from September to November) and usually last about a week. They are interrupted by weak southerlies or, less frequently, northerlies [*Garreaud and Muñoz*, 2005].

[3] The LLCJs are highly variable with different temporal [*Pizarro et al*., 2001, 2002; *Dewitte et al*., 2008; *Renault et al*., 2009] and spatial scales [*Renault et al*., 2009]. *Jiang et al*. [2010] has separated the LLCJs into two types: a strong-forcing jet, with the SEPH close to the central Chilean coastline; and a weak-forcing jet, with the SEPH centered far away from the coastline. For the strong-forcing jet period, the mean SEPH is centered near 95°W, ~2000 km offshore. The LLCJ is approximately 1500 km in length, located between 25° and 40°S with a surface maximum near 36°S. For the weak-forcing jet period, the mean center of the SEPH is located to the west of 110°W and the surface pressure gradient offshore of central Chile is noticeably weaker than the strong-forcing jet period. The surface LLCJ is substantially shorter in length, weaker in strength, and centered farther north compared to the strong-forcing jet period. The study found that the strong (weak)-forcing jet is much more (less) intense and associated with stronger (weaker) interaction between the SEPH and the Andes, and the impact of land-sea differential heating on the LLCJ is in general smaller (larger).

[4] The mechanism for the sea-surface temperature (SST) modification by the LLCJ may not be exactly the same for different LLCJ events. For example, for a particular coastal jet event observed from 3 to 15 October 2000, the ocean response consists of a cooling in the jet core area that is mainly driven by a combination of heat fluxes and advection of upwelled waters. However, for another coastal jet event observed from 7 to 15 January 2003, the Ekman pumping contribution to the cooling is stronger than the event during the October 2000. *Renault et al*. [2009]

[1]Naval Research Laboratory, Monterey, California, USA.
[2]Naval Research Laboratory, Stennis Space Center, Mississippi, USA.
[3]College of Earth and Atmospheric Sciences, Oregon State University, Corvallis, Oregon, USA.

Corresponding author: X. Hong, Naval Research Laboratory, 7 Grace Hopper Avenue, Monterey, CA 93943, USA. (hong@nrlmry.navy.mil)

2169-9275/13/10.1002/jgrc.20289

indicated that the differences in the preferential cooling processes for the two events are attributed to the different mean atmospheric and oceanic conditions and to the different characteristics of the coastal jets such as location of the jet core and intensity.

[5] On the other hand, for the same LLCJ event observed from 3 to 15 October 2000, the two studies [*Renault et al*., 2009, 2012] show differences in the results and derive different mechanisms. These differences may be due to the limitation in the observational data sets [*Renault et al*., 2009] or the boundary conditions for forcing the atmospheric model [*Renault et al*., 2012]. Especially for the coastal zone, the wind dropoff (i.e., the sharp weakening of coastal winds toward the shore) is important for the coastal upwelling and Ekman pumping and needs to be represented correctly. Overestimating (underestimating) the wind dropoff zone would result in overestimating (underestimating) Ekman pumping and underestimating (overestimating) coastal upwelling. Previous studies show that coastal SST is the main forcing of wind dropoff by changing the marine boundary layer (MBL) depth [*Jin et al*., 2009]. As shown in *Renault et al*. [2012], a poorly resolved coastal zone by the Tropical Rainfall Measuring Mission (TRMM) Microwave Imager (TMI) SST can result in an inaccurate representation of the wind dropoff due to its physical forcing. This suggests that using a fully coupled mesoscale air-ocean modeling system would be crucial to account for more realistic wind-SST interaction and provide better wind dropoff representation, in addition to its ability to better capture small-scale coastal features in the alongshore wind [*Capet et al*., 2004; *Renault et al*., 2012]. In addition, the daily updated SST is not suitable for the short time scale events such as the coastal jet event. This could induce large bias for the surface heat fluxes that will force the ocean model simulation subsequently. The uncoupled simulation in *Renault et al*. [2012] also show bias in the estimation of turbulent heat fluxes since the atmospheric stability conditions are associated with the air-sea temperature difference, which can be better provided from the coupled simulation.

[6] Based on this motivation, we use a two-way fully coupled model COAMPS® (Coupled Ocean/Atmosphere Mesoscale Prediction System, COAMPS is a registered trademark of the Naval Research Laboratory) to study air-sea interaction of the LLCJ and the modification of SST during the Variability of the American Monsoon System (VAMOS) Ocean-Cloud-Atmosphere Land Study Regional Experiment (VOCALS-REx, Wood and the VOCALS Scientific Working Group, 2010) from 20 October to 30 November 2008 in the SEP region. Furthermore, previous studies of SST change associated with LLCJ over the SEP area only focus on the strong-forcing jet periods [*Renault et al*., 2009, 2012]. To gain more understanding and provide full insight of the impact of highly variable and complex LLCJ on the SST change over the SEP area, it is necessary to investigate various LLCJ events, including not only for the strong-forcing jet periods but also for the weak-forcing jet periods, which is lacking in previous studies [*Renault et al*., 2009, 2012].

[7] Section 2 briefly describes COAMPS and the model configuration. Section 3 compares the variability and characteristics of the LLCJ using model results and observations. Section 4 describes the SST changes during the strong and weak jet periods. Section 5 discusses the important roles played by the different processes related to the LLCJ. Section 6 presents the summary and conclusions.

2. Description of COAMPS Components and Configuration

[8] Two-way coupled COAMPS has been evaluated extensively for different areas and objectives. Detailed information regarding the coupling method can be found in *Chen et al*. [2010] for studying the effect of two-way air-sea coupling in high-wind and low-wind speed regimes and in the validation report of *Allard et al*. [2010] for verifications associated with Adriatic Sea circulation, Ligurian air-sea interaction, autonomous ocean sampling network (AOSN)-Monterey Bay, Kuroshio extension system, and VOCALS experiment. Here, we only briefly describe the different components that comprise the two-way coupled COAMPS.

2.1. Atmospheric Model

[9] The COAMPS atmospheric component is a fully compressible, nonhydrostatic, primitive-equation model based on a staggered, C grid and is solved using a time-splitting technique with a semi-implicit formulation for the vertical acoustic modes [*Hodur*, 1997; *Hodur et al*., 2002]. A Robert time filter is used to damp the computational mode. All derivatives are computed to second-order accuracy and options are provided for fourth-order accurate horizontal advection and diffusion. The surface fluxes are computed following a hybrid scheme described by *Wang et al*. [2002], which combines both the *Louis et al*. [1982] and *Fairall et al*. [2003] formulations, which make use of Monin-Obukhov similarity theory. A force-restore method is used to parameterize the surface energy budget. The subgrid-scale moist convective processes are parameterized using an approach following *Kain and Fritsch* [1990]. The grid-scale evolution of the moist processes is explicitly predicted from budget equations for cloud water, cloud ice, rain, snow, and water vapor [*Rutledge and Hobbs*, 1983]. The parameterization of shortwave-radiation and longwave-radiation processes is accomplished following *Harshvardhan et al*. [1987]. The planetary boundary layer and free-atmospheric turbulent mixing and diffusion are modeled using a prognostic equation for the turbulent kinetic energy (TKE) budget based on a method derived from the level 2.5 formulation of *Mellor and Yamada* [1982]. COAMPS can use an arbitrary number of terrain-following vertical levels.

[10] A three-dimensional, multivariate, optimum-interpolation (MVOI), analysis technique is used to map the observations to the model grid and generate the initial conditions for the forecast model for each data assimilation cycle. Quality-controlled data used in the analysis are radiosonde, aircraft, satellite, and surface observations.

2.2. Ocean Model

[11] The Navy Coastal Ocean Model (NCOM) is used for the ocean component of the coupled system and is a three-dimensional, primitive-equation, free-surface model using the hydrostatic, Boussinesq, and incompressible approximations [*Martin*, 2000]. NCOM is designed to offer

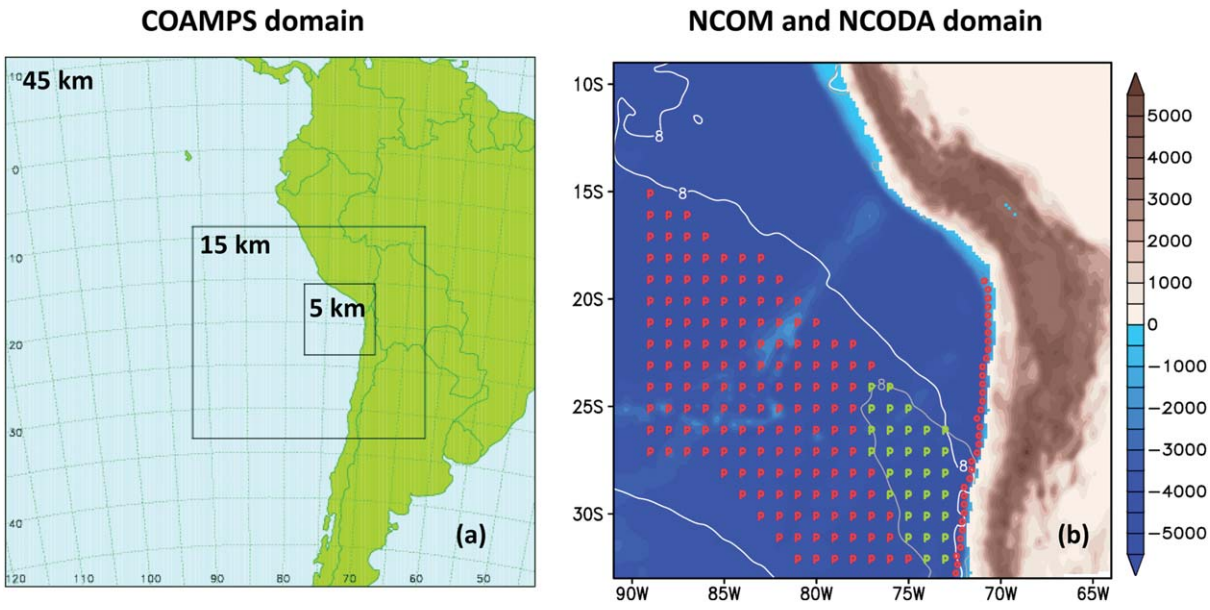

Figure 1. (a) COAMPS nested atmospheric grids (with 45, 15, and 5 km resolution) and (b) the 15 km resolution NCOM/NCODA grid. In Figure 1b, terrain and bathymetry are shown in color shades (units = meters). The white contour lines denote the mean wind speed of 8 m s^{-1} for three strong-forcing jets from 29 to 30 October 2008 and the gray contour line is for the weak-forcing jet from 22 to 23 November 2008. In Figure 1b, the marks "O" along the coast and "P" along the jet path, in which "P" marks (both green and red) are for strong-forcing jet and green "P" marks are for the weak-forcing jet, are used as locations of coast and jet path grid for Figure 17.

the user a range of numerical choices in terms of parameterizations, numerical differencing, and vertical grid structure. The model equations are solved on a staggered, Arakawa C-grid. Temporal differencing is leap-frog with an Asselin filter to suppress time splitting. Spatial averages and finite differences are mainly second order with an option for higher-order formulations for advection. The propagation of surface waves and vertical diffusion is treated implicitly. The Mellor-Yamada Level 2.5 turbulence scheme [*Mellor and Yamada*, 1982] is used for vertical mixing. NCOM forcing includes surface air-sea fluxes, lateral open-boundary conditions, tides, and river and runoff discharges [*Hong et al*., 2009a].

[12] NCOM has an orthogonal-curvilinear horizontal grid and a hybrid sigma and *z*-level vertical grid with sigma coordinates applied from the surface down to a specified depth and with level coordinates used below the specified depth. The bathymetry used is from the NRL 2 min resolution Digital Bathymetric Data Base (DBDB2).

2.3. NCODA

[13] The Navy Coupled Ocean Data Assimilation (NCODA) system used here is a fully three-dimensional, multivariate, optimum-interpolation (MVOI) ocean data assimilation system that produces simultaneous analyses of temperature, salinity, geopotential (dynamic height), and vector velocity. A complete description of NCODA can be found in *Cummings* (2005) and an application of NCODA in a coastal field campaign is described in *Hong et al*. [2009b]. Observations used in the ocean analysis include all sources of operational ocean observations. They contain remotely sensed SST from *Advanced Very High Resolution Radar Global Area Coverage* (AVHRR GAC) infrared satellite, sea-surface height from satellite altimeters, in situ surface and subsurface observations of temperature and salinity from a variety of sources, such as ships, buoys, expendable bathythermographs, and conductivity-temperature-depth sensors. A description of the operational data sources can be found in *Cummings* [2005, Table 1]. These data have been quality controlled and archived in the Global Ocean Data Assimilation Experiment (GODAE) server hosted by the Fleet Numerical Meteorology and Oceanography Center (FNMOC).

2.4. Coupling and Configuration

[14] For the coupled and uncoupled simulations, the atmospheric model provides a total of six fields to force NCOM: sea-level pressure, surface wind stress in the *x* and *y* directions, total heat and moisture fluxes, and net solar radiation. The SST for the atmospheric model is initially provided by the NCODA analysis. For the two-way coupled simulation, the SST is forced by NCOM every 30 min during the integration. For the uncoupled simulation, the two-dimensional NCODA SST analysis is held constant for the entire 48 h forecast length.

[15] The coupled and uncoupled simulations were run twice daily using a 12 h data assimilation update cycle for both atmospheric and oceanic components such that each forecast was initialized using a first-guess analysis from the previous 12 h forecast combined with current observational data using an MVOI scheme.

[16] The COAMPS atmospheric model setup for this study is triply nested and uses a Lambert conformal grid projection (Figure 1). The horizontal resolutions of the

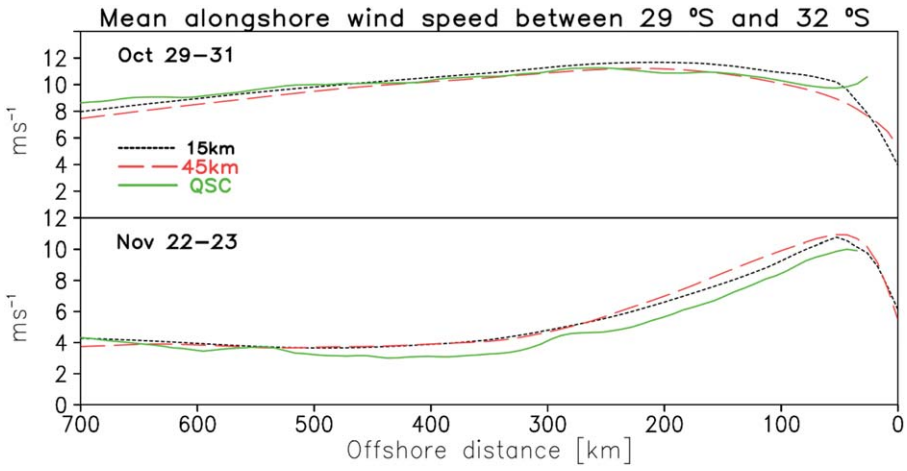

Figure 2. Mean COAMPS and QuikSCAT surface alongshore wind speed between 29°S and 32°S for (a) the strong-forcing jet from 29 to 30 October and (b) the weak-forcing jet from 22 to 23 November 2008.

three nested grids are 45, 15, and 5 km, with horizontal grid dimensions of 151 × 151, 199 × 181, and 181 × 181 points, respectively. There are 45 sigma levels in the vertical with 15 levels in the lowest 1000 m. The NCOM and NCODA domains have the same size and resolution in the horizontal as the second COAMPS grid, and use 41 and 30 levels in the vertical, respectively. There are 16 levels within 100 m depth for the NCOM simulation. The COAMPS domain settings were used for a real-time forecast of MBLs during VOCALS-Rex [*Wang et al*., 2011]. Intensive observations were carried out along latitude 20°S during the field experiment to provide detailed time-height and longitude-height cross sections of the MBL. Therefore, the comparison between the model forecasts and observations primarily used the model output from nest 3 (5 km resolution) [*Wang et al*., 2011]. In this study, however, only results from nest 2 (15 km resolution) are analyzed for the purpose of investigating SST changes along the Peruvian and Chilean coast due to air-sea interaction through the variability of the coastal jet.

2.5. Wind Dropoff

[17] *Capet et al*. [2004] has demonstrated that high-resolution COAMPS forcing for coastal oceanic modeling contains mesoscale wind structure and can significantly influence nearshore circulation. However, the wind profile does not seem to converge as its resolution increases, as found in other numerical models. The wind dropoff scale decreases with the grid scale in COAMPS surface wind [*Capet et al*., 2004] in contrast with the Weather Research Forecast (WRF) model surface wind, which shows that the wind dropoff is insensitive to model resolution [*Renault et al*., 2012]. The current status of wind dropoff in the new two-way coupled version of COAMPS used for this study is examined here.

[18] Figure 2 shows mean COAMPS and QuikSCAT surface alongshore wind speeds between 29°S and 32°S for the strong-forcing jet from 29 to 30 October (Figure 2a) and the weak-forcing jet from 22 to 23 November (Figure 2b). The simulated wind speeds are comparable with satellite observations. Stronger wind dropoff for the weak-forcing jet and weaker wind dropoff for the strong-forcing jet is evident in both COAMPS and observations. Although there is still not absolute convergence with model resolution, the improved COAMPS wind profiles in Figure 2 provide similar wind dropoff between two different model resolutions. The wind dropoff scales (∼70 km) from both model resolutions are also consistent with WRF output, although the WRF output may also have some degree of inaccuracy due to its use of TMI SST for physical forcing for the lower boundary condition for the atmospheric model [*Renault et al*., 2012]. In the two-way coupled modeling, the physical process between SST and wind coupling is included so that the MBL thickness can be better simulated. The two-way coupled model can also better represent other factors that contribute to the wind dropoff such as sharp horizontal changes in surface drag and atmospheric boundary layer at the land-sea interface [*Edwards et al*., 2001; *Capet et al*., 2004].

3. Characteristics of the Strong-Forcing and Weak-Forcing Jets

[19] The formation and dynamics of the LLCJ events during the VOCALS-Rex period have been examined by *Jiang et al*. [2010] using an uncoupled atmospheric model simulation and additional sensitivity simulations. There are four LLCJ events during this period with three strong-forcing LLCJ and one weak-forcing LLCJ. Here, we have selected the event from 29 to 30 October 2008 for our study, since it is the strongest among the three strong-forcing jet cases and we will compare the results with the weak-forcing jet case from 22 to 23 November 2008.

[20] Some characteristics of the two LLCJ events from the two-way coupled simulation are displayed and compared with those from the uncoupled simulation (Figure 3). The 1022 hPa sea-level pressure contour (black-dashed lines) indicates the position of SEPH and its relation to the LLCJ. During the strong-forcing jet period from 29 to 30 October (Figures 3a–3c), the mean SEPH moves eastward and a strong northerly directed pressure gradient forces the LLCJ along the Chilean coast. The 8 ms^{-1} contour lines of

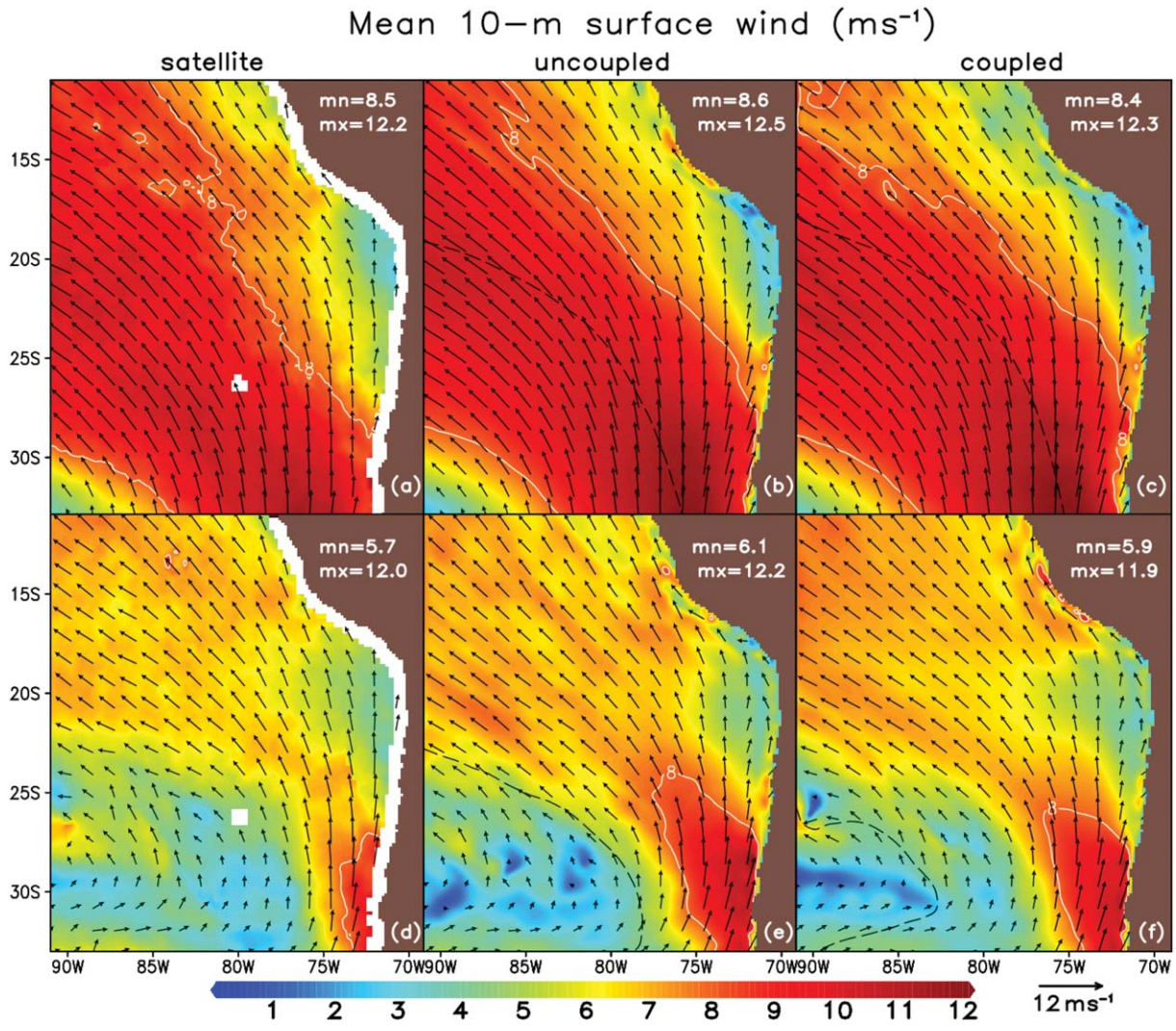

Figure 3. Mean 10 m surface wind from satellite (left), uncoupled (middle), and coupled (right) simulations (top) for strong-forcing jet from 29 to 30 October and (bottom) for weak-forcing jet from 26 to 29 November. The vectors are plotted every eight grid points for clarity. The white contour lines are wind speeds of 8 m s^{-1}. The black-dashed lines are sea-level pressure of 1022 hPa, denoting the extension of the SEPH. The domain-mean (mn) and domain-maximum (mx) are given in the top-right corner of each plot. The satellite wind speeds (left) (color-shaded) are from four passive microwave radiometers (AMSR-E, TRMM TMI, SSM/I F13, and F15 satellites) and the wind vectors are QuikSCAT.

wind speed indicate the jet with wind direction northward along the central Chilean coast and then northwestward offshore. This strong-forcing jet occurring from 29 to 30 October has similar strength and coverage to the one from 3 to 15 October 2000 and studied by *Renault et al*. [2009, 2012], with the jet center also located near 36°S from surface wind in nest 1 (figure not shown). The area of wind speeds exceeding 8 ms^{-1} occupies about 70% of the domain. During the weak-forcing jet period from 22 to 23 November (Figures 3d–3f), the mean center of SEPH moves offshore to the west, the LLCJ, as one of the circulation branches around the SEPH center, becomes weaker and is located further north at ∼32°S. Although the maximum wind speed is comparable along the Chilean coast, the area of wind speeds excedding 8 ms^{-1} is reduced significantly (Figures 3d–3f), to only about 10% of the domain (Figures 3a–3c). The domain-mean wind speed is only 5.9 ms^{-1} from the coupled simulation, about 30% smaller than the strong-forcing jet.

[21] The coupled simulation in general has smaller maximum and domain-mean wind speeds (Figure 4a) and is generally better simulated statistically than the uncoupled simulation (Figure 5a). For example, the overall absolute bias, which is defined as the absolute sum for all biases from domain-mean and domain-maximum biases, is 0.5 ms^{-1} for surface wind speed for the coupled simulation (50% less) and 1.0 ms^{-1} for the uncoupled simulation.

[22] The air mass associated with the strong-forcing jet is much cooler and drier than the weak-forcing jet. Comparing Figures 6a and 6b for the two jet scenarios, the domain-mean 2 m air temperature is −1.3°C less for the strong-forcing jet period than the weak-forcing jet period

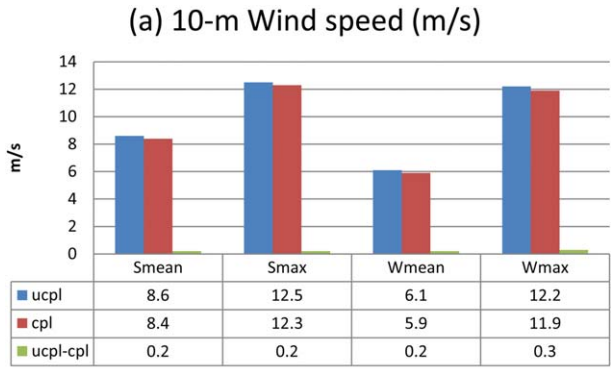

	Smean	Smax	Wmean	Wmax
ucpl	8.6	12.5	6.1	12.2
cpl	8.4	12.3	5.9	11.9
ucpl-cpl	0.2	0.2	0.2	0.3

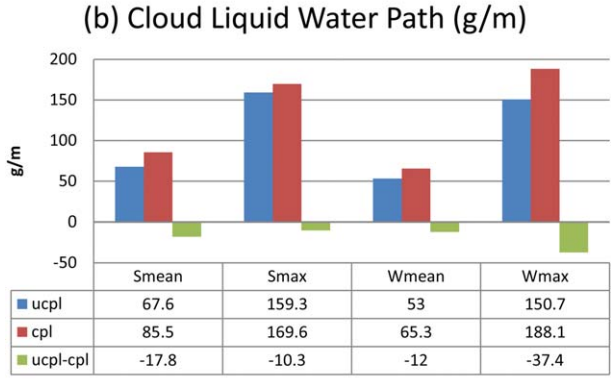

	Smean	Smax	Wmean	Wmax
ucpl	67.6	159.3	53	150.7
cpl	85.5	169.6	65.3	188.1
ucpl-cpl	-17.8	-10.3	-12	-37.4

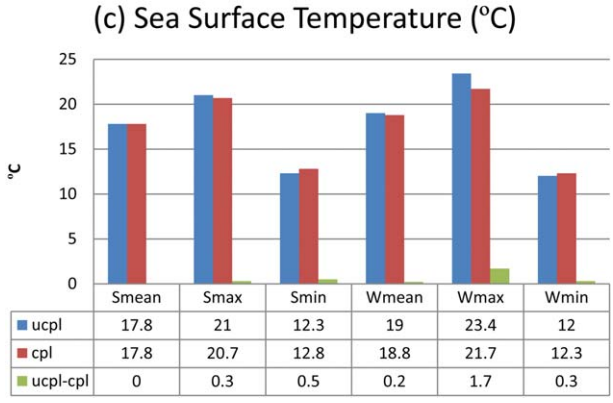

	Smean	Smax	Smin	Wmean	Wmax	Wmin
ucpl	17.8	21	12.3	19	23.4	12
cpl	17.8	20.7	12.8	18.8	21.7	12.3
ucpl-cpl	0	0.3	0.5	0.2	1.7	0.3

Figure 4. Domain-mean, domain-maximum, and domain-minimum during the strong-forcing (29–30 October) and weak-forcing (22–23 November) jet periods for the uncoupled, coupled simulations, and their differences.

(16.6–17.9 = −1.3°C). The southeast area in Figure 6a is the coldest in response to the strongest wind shown in Figure 3c and also has the coldest water (shown in Figure 8c), due to the wind-induced upwelling. The domain-mean air-temperature anomaly from the 41 day mean is negative (−0.7°C) during the strong-forcing jet period and positive (0.6°C) during the weak-forcing jet period, further indicating the negative correlation between the air temperature and the strength of the coastal jet. This negative correlation also occurs for the water vapor (Figures 6c and 6d). The anomaly of the water vapor mixing ratio averaged over the domain is -0.8 g kg^{-1} for the strong-forcing jet period and 0.2 g kg^{-1} for the weak-forcing jet period. The dry character of the strong-forcing jet is more pronounced in the southern part of the domain. The domain-mean difference of the water vapor mixing ratio between the strong-forcing and weak-forcing jet periods in this area is more than -1.1 g kg^{-1}.

[23] The LLCJ formation is associated with the quasi-permanent SEPH system. Its southern branch brings cold and dry air from high-latitudes and reaches the central Chilean coastal area. Therefore, the strong jet brings more cold and dry air masses and forms colder and drier air over the SEP than a weak jet. This induces cold and dry anomalies as seen in Figures 6a and 6c. When the jet is weak, less cold and dry air masses are brought to the SEP, and the local forcing becomes dominant. More moist and radiation heat flux transfer occurs from the ocean to the air, resulting in warm and moist anomalies during the weak-forcing jet period.

[24] The uncoupled results show in general warmer and drier air for both strong-forcing and weak-forcing jet periods, indicated by the domain-maximum and domain-minimum for temperature and domain-minimum for the water vapor when compared with the coupled simulation. Overall, mean differences of minimum air temperature between the coupled and uncoupled simulations are ∼0.6–0.8°C.

[25] The cold air carried by the strong jet increases the lower-troposphere stability, which limits the entrainment of dry air from above the MBL. This feature, combined with descending warmer air from the strong temperature inversion at the top of the MBL due to the large-scale subsidence and results in more stratocumulus clouds across the area. This is evident in the cloud liquid water path (CLWP) for the strong-forcing jet (Figures 7a–7c) as compared to the weak-forcing jet (Figures 7d–7f). About 80% of the domain is covered by clouds (based on the CLWP being larger than ∼60 g m^{-2}) during the strong-forcing jet period but less than 40% of the domain is covered by clouds during the weak-forcing jet period. This is because the warmer air and SST during the weak-forcing jet period causes a decrease in the lower-troposphere stability and eventually leads to the entrainment of dry air into the cloud deck and the replacement of stratus clouds with cumulus [*Wyant et al.*, 1997; *Wood and Hartmann*, 2006; *Clement et al.*, 2009]. The coastal clearing associated with the jet shown in the previous studies [*Garreaud and Munoz*, 2005; *Renault et al.*, 2012] can be seen in Figure 7 for both the strong-forcing and weak-forcing jets but with different coverage.

[26] Although there are less model-simulated clouds as compared to observations due to the lower model-simulated MBL heights in the model [*Wang et al.*, 2011], the model does provide adequate cloud coverage, with a relatively thick clouds covering the western part of the domain and thinner clouds along the coast. In particular, the coupled simulation provides more clouds (Figure 4b) and better agreement with observations than the uncoupled simulation since both domain-mean and maximum CLWP are larger. The overall absolute bias from the coupled simulation is about 30% of that from the uncoupled simulation (Figure 5b). An accurate simulation of clouds is critically important since it affects the solar and longwave radiation absorbed by the ocean. The clouds also influence large-scale weather systems, which in turn affect the ocean through surface wind stresses.

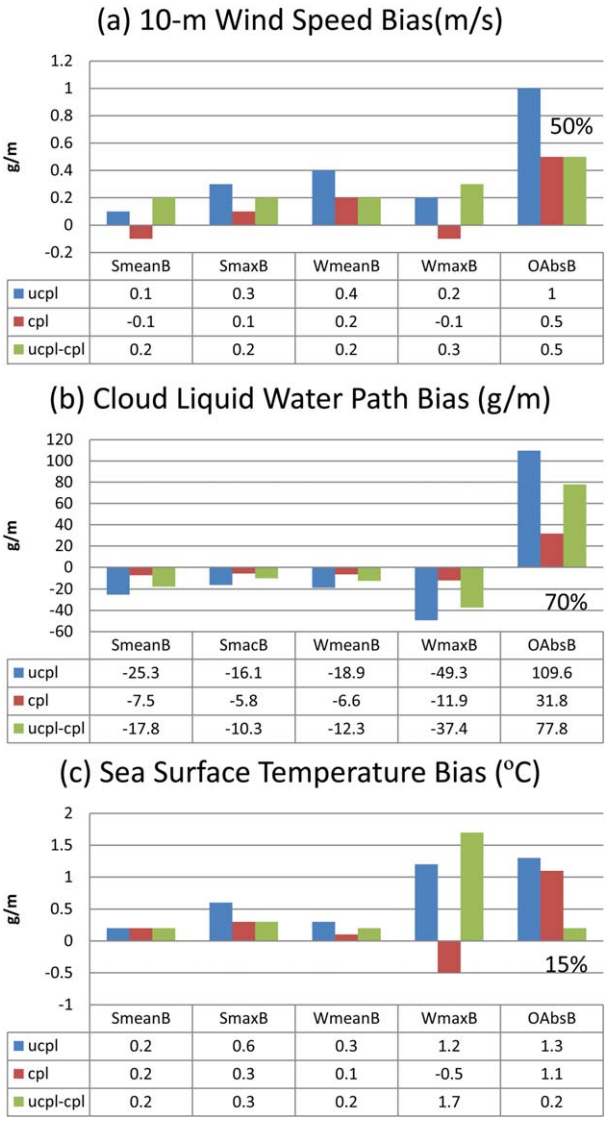

Figure 5. Biases for the domain-mean and domain-maximum during the strong-forcing (29–30 October) and weak-forcing (22–23 November) jet periods. The last column is the overall absolute bias (OAbsB), which is the absolute sum for all biases in the same row. The percentage near this category denotes the bias reduced by the coupled simulation relative to the uncoupled simulation. Note: The statistics are computed using available satellite observations for the surface wind, CLWP, and SST. There is a narrow fringe of 25 km along the coast without data as seen in Figures 3a and 3d, Figures 7a and 7d, and Figures 8a and 8d. Therefore, the model validation does not include this coastal blind zone. The domain-minimum SST bias is not included in Figure 5 since the coldest SST is within the blind zone (Figures 8a and 8d).

4. SST Responses During the Strong-Forcing and Weak-Forcing Jet Periods

[27] The SST responds to the coastal jet significantly and differentially in magnitude and spatial pattern due to the variability of jet in strength, time, and location. To show this, the features of the SST from the selected strong-forcing and weak-forcing jet periods are presented in Figure 8. The SST decreases relative to its mean during the strong-forcing jet period and increases during the weak-forcing jet period, as also noted by others [*Soto-Mardones et al*., 2004; *Albert et al*., 2010]. The warm SST near the coastline curvature between Chile and Peru is due to the weak meridional winds that are unable to produce upwelling [*Soto-Mardones et al*., 2004]. The largest decrease of SST is located along the coast of central Chile and the cooler water extends offshore to replace the warm water (Figures 8a–8c). The model results (Figures 8b and 8c) show SST patterns similar to the observations from AMSR-TMI (Figure 8a). The cool model SST in the model extends farther offshore from the coast but less north from the center of the cold water. Colder SST along the central Chile coast is due to the stronger maximum wind in this area that induces more upwelling. The model SST over the entire area is generally warmer than observed due to less cloud coverage, resulting in a domain-mean SST change larger than observed and a model warm bias of 0.2°C for both coupled and uncoupled simulations (Figure 5c).

[28] During the weak-forcing jet period, the offshore under SEPH center warm SST retreats to the coast and replaces the coastal cold water as evident in both the observations (Figure 8d) and the model (Figures 8e and 8f). The areas covered by cold water are much smaller than during the strong-forcing jet period. Large minimum temperature differences between observations and model are caused by the lack of observations along the coast. The SST increases more significantly in the north since more solar radiation is absorbed near the equator. The larger warm bias from the domain-mean SST in the uncoupled simulation is due to significantly reduced clouds as shown in Figure 7e.

[29] The larger cold bias for the domain-minimum SST from the uncoupled simulation (Figure 4c) is due to stronger domain-maximum wind speed along the Chilean coast, which induces more upwelling. The coupled simulation shows an overall absolute bias for the domain-mean and domain-maximum reduced to 26% of the bias from the uncoupled simulation (Figure 5c).

5. Important Processes Affecting SST Modulation

[30] Four major processes, Ekman pumping, horizontal advection, vertical entrainment, and net surface heat flux exchange have various impacts on the SST change over the SEP area according to the previous studies [*Halpern*, 2002; *Soto-Mardones et al*., 2004; *Renault et al*., 2009, 2012; *Albert et al*., 2010]. The Ekman pumping due to divergence and convergence of the Ekman transport are responsible for the upwelling and downwelling processes affecting the SST change. Horizontal advection changes the SST due primarily to transport of cold upwelled water offshore. The vertical entrainment is sensitive to the wind-induced mixing and surface buoyancy forcing that vary between strong-forcing and weak-forcing jets. The net surface heat flux, consisting of the shortwave and longwave radiation and the latent and sensible heat fluxes, is affected by the variability of the LLCJ and modifies the SST directly through air-ocean heat exchange.

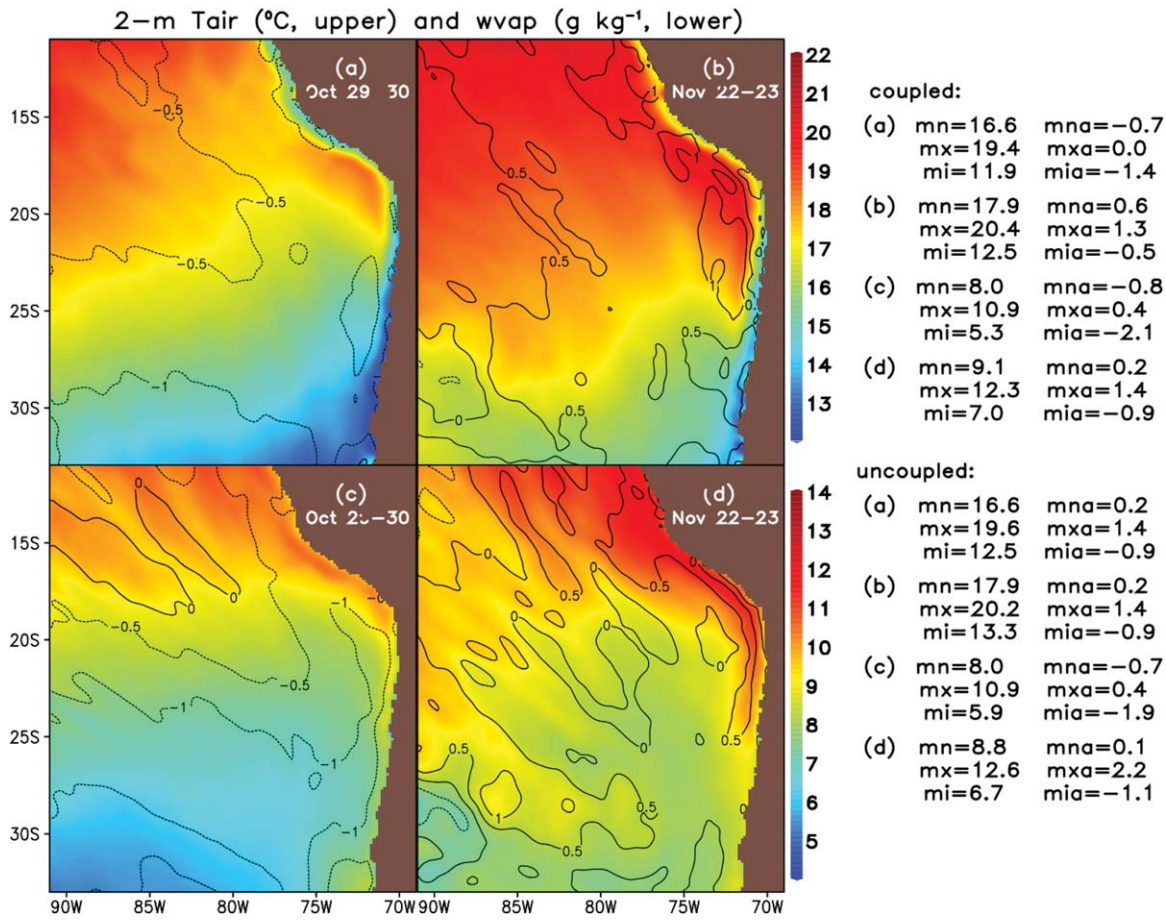

Figure 6. Coupled 2 m (top) air temperature (°C) and (bottom) water vapor (g kg^{-1}) for the strong-forcing jet (left) and weak-forcing jet (right). The mean and anomaly are in color shaded and contour, respectively. The domain-mean (mn), domain-maximum (mx), and domain-minimum (mi) and the anomaly domain-mean (mna), anomaly domain-maximum (mxa), and anomaly domain-minimum (mia) from the coupled and uncoupled simulations are shown in the right.

5.1. Impact of Upwelling

[31] The rate of temperature change at the surface due to the upwelling or downwelling can be estimated as:

$$\left.\frac{\partial T}{\partial t}\right|_{upw} = -w_e \frac{\partial T}{\partial z}, \tag{1}$$

where T is temperature, t is time, z is the vertical coordinate, and w_e is the upwelling or downwelling speed (given in equation (2)). The vertical gradient of temperature $\frac{\partial T}{\partial z}$ in equation (1) is estimated from the difference of the temperature at the surface and the base of the mixed layer. The mixed-layer depth (H_m) is defined as the depth where the potential density difference with respect to the value at the surface exceeds 0.01 kg m^{-3} [*Thomson and Fine*, 2003]. The mixed-layer depth differs significantly between the strong-forcing and weak-forcing jet periods (Figures 9a and 9b). Less (more) stable ocean surface conditions during the strong (weak) forcing jet period result in much more (less) vertical mixing and deeper (shallower) mixed-layer depths.

[32] The vertical gradient of temperature is important in the calculation of the rate of temperature change by the Ekman pumping, since it provides the precondition for the surface cooling. The strong-forcing jet period selected here is during October, which has several synoptic disturbances as discussed in *Wang et al*. [2011] and in *Rahn and Garreau* [2010]. Frequent occurrences of the coastal jet creates more opportunities for coastal upwelling and vertical mixing due to surface heat loss, which reduces the vertical gradient of temperature (Figure 9c) and supplies weak preconditioning for changes in the surface temperature. On the other hand, during November, weak synoptic disturbances and seasonal warming result in higher SSTs, which increase the vertical gradient of temperature as shown in Figure 9d. The negative vertical gradient occupies the whole domain during the weak-forcing jet period, with a maximum of -0.13°C m^{-1} and a domain mean of -0.03°C m^{-1}, which exceeds the corresponding values during the strong-forcing jet period. The small positive value along the jet path in Figure 9c indicates the surface cooling induced by the air-sea heat flux exchange during the strong-jet period.

[33] The upwelling or downwelling speed w_e can be computed as [*Gill*, 1982; *Halpern*, 2002]:

$$w_e = \frac{\partial u_e}{\partial x} + \frac{\partial v_e}{\partial y}. \tag{2}$$

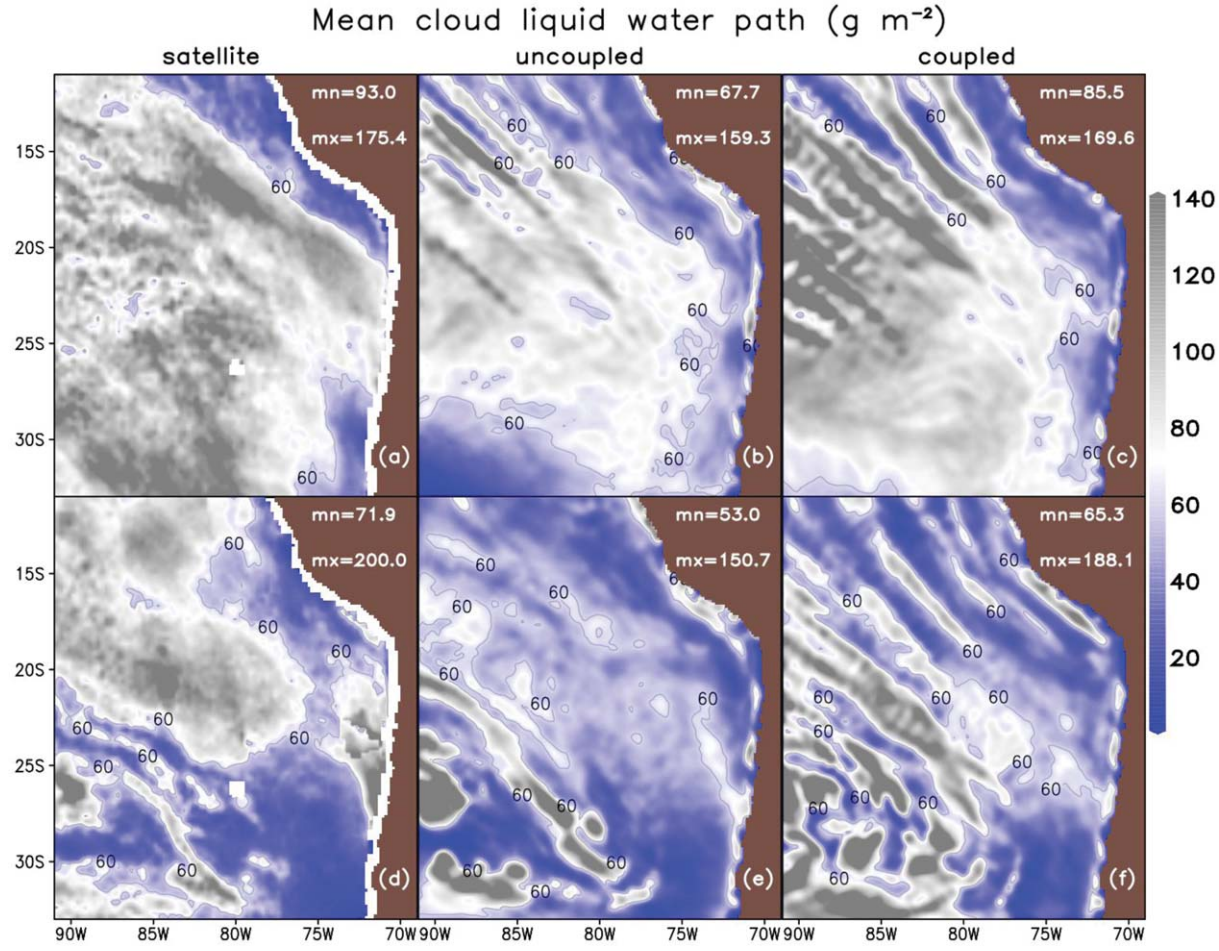

Figure 7. As in Figure 3 but for cloud liquid water path (CLWP).

where u_e and v_e are the x-component and y-component of the Ekman volume transport and defined by *Gill* [1982] and *Pickett and Paduan* [2003] as:

$$(u_e, v_e) = \frac{1}{\rho_w f}\boldsymbol{\tau} \times \mathbf{k}, \tag{3}$$

where u_e and v_e are the x-component and y-component of the Ekman volume transport, $\boldsymbol{\tau}$ is the surface wind stress forecast by the atmospheric model, $\rho_w = 1024$ kg m^{-3} is the density of seawater, $f = 2\Omega \sin\theta$ is the Coriolis parameter, $\Omega = 7.292 \times 10^{-5}$ s^{-1} is the Earths angular velocity, θ is the latitude, and $\mathbf{k}$ is the unit vertical vector. If we substitute equation (3) into equation (2) we get:

$$w_e = \frac{\nabla \times \boldsymbol{\tau}}{\rho_w f} + \frac{\beta \tau_x}{\rho_w f^2}, \tag{4}$$

where $\nabla \times \boldsymbol{\tau}$ is the wind stress curl and β is the latitudinal variation of the Coriolis parameter. Note that the second term in equation (4) is about two orders of magnitude smaller than the first term in our calculation (not shown). Equations (2) and (4) show that the upwelling or downwelling speed at the base of the Ekman layer is due to the horizontal divergence or convergence of the Ekman transport, which is due to the curl of the wind stress. Along a western coast in the Southern Hemisphere, negative wind stress curl induced by the equatorward wind stress is favorable for upwelling through the Ekman pumping process [*Halpern*, 2002*; Albert et al*., 2010].

[34] Strong cooling induced by the upwelling from the coupled simulation is concentrated along the central Chilean coast and south Peruvian coast (Figure 10b), which is consistent with the locations of maximum negative wind stress curl (figure not shown) and upwelling velocity (figure not shown). The cooling extends offshore and covers the half of the domain area where the upwelling occurs. The maximum cooling rate is -0.13°C d^{-1} during the strong-forcing jet period, which is actually less than that during the weak-forcing jet period (-0.23°C d^{-1}). This is due to the larger vertical temperature gradient during the weak-forcing jet period (Figures 9c and 9d). The cooling area is much smaller during the weak-forcing jet period as expected; therefore, there is a smaller domain-mean rate of temperature change. The uncoupled simulation shows stronger maximum cooling than the coupled simulation with the range of differences of minimum temperature from 0.02 to 0.08°C d^{-1}. The stronger cooling is consistent

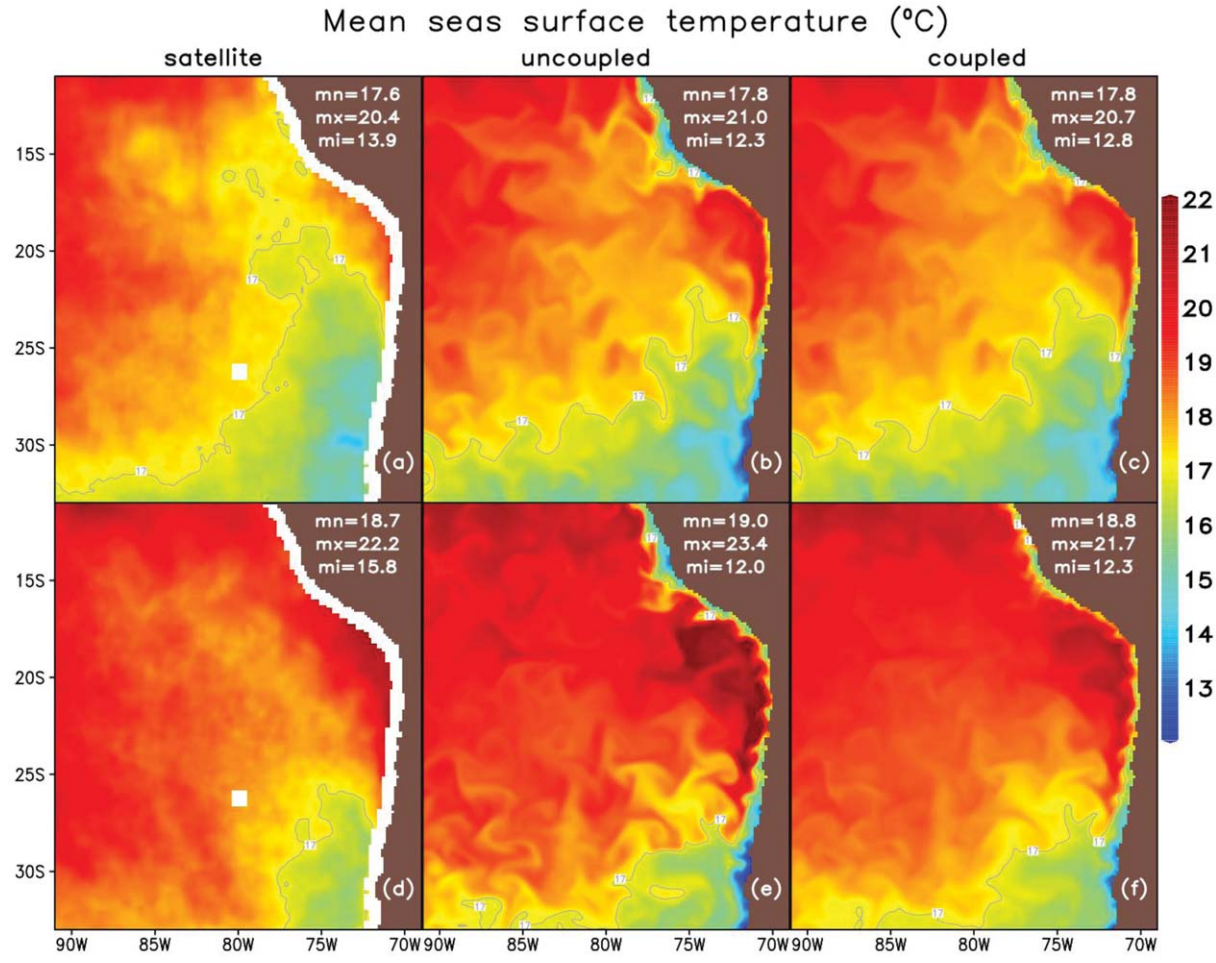

Figure 8. As in Figure 3 but for mean SST. The domain-mean (mn), domain-maximum (mx), and domain-minimum (mi) values are given in the top-right corner of each plot. The satellite observed SST (left) is from AMSR-E and TMI.

with the stronger maximum wind from the uncoupled simulation (Figures 3b and 3e).

[35] The cooling induced by the upwelling is concentrated along the coastal area, similar to the results of *Renault et al.* [2012]. However, more fine structures and stronger cooling from both coupled and uncoupled simulations are presented in the present study. This could be caused by computing the mean over a longer duration, i.e., 12 days in *Renault et al.* [2012] but only 3 days in the current study.

5.2. Impact of Horizontal Advection

[36] Seaward advection of temperature resulting from Ekman transport is significant in a long-term mean process. It provides net warming (cooling) in the region north (south) of 20°S [*Zheng et al.*, 2010]. Although geostrophic transport may also contribute to the SST change, for the strong southerly wind along the coast over SEP area, the role for the Ekman transport is enhanced in horizontal advection. We will examine the Ekman advective heat flux to emphasize the role for the Ekman transport but the SST change will be from the total horizontal advection.

[37] The advective heat flux due to the Ekman transport is given by

$$Q_{ek} = C_{pw}\rho_w\left(u_e\frac{\partial T}{\partial x} + v_e\frac{\partial T}{\partial y}\right) \tag{5}$$

where $C_{pw} = 4185.5\ \mathrm{J\ kg^{-1}\ K^{-1}}$ is the heat capacity of seawater. The Ekman velocity is the vertically averaged velocity within the Ekman layer [*Yang*, 2006]:

$$u_{ek} = \frac{u_e}{H_{ek}} \tag{6a}$$

$$v_{ek} = \frac{v_e}{H_{ek}} \tag{6b}$$

[38] The depth of the Ekman layer H_{ek} can be obtained as in *Soto-Mardones et al.* [2004]

$$H_{ek} = \kappa\frac{u_*}{f}, \tag{7}$$

where von Kármán's constant κ is taken to be equal to 0.42 [*Ruggles*, 1970]. The friction velocity u_* is output from the coupled model. It is calculated from the 10 m wind speed and Richardson number, which is determined by the vertical wind shear and stability [*Louis*, 1979].

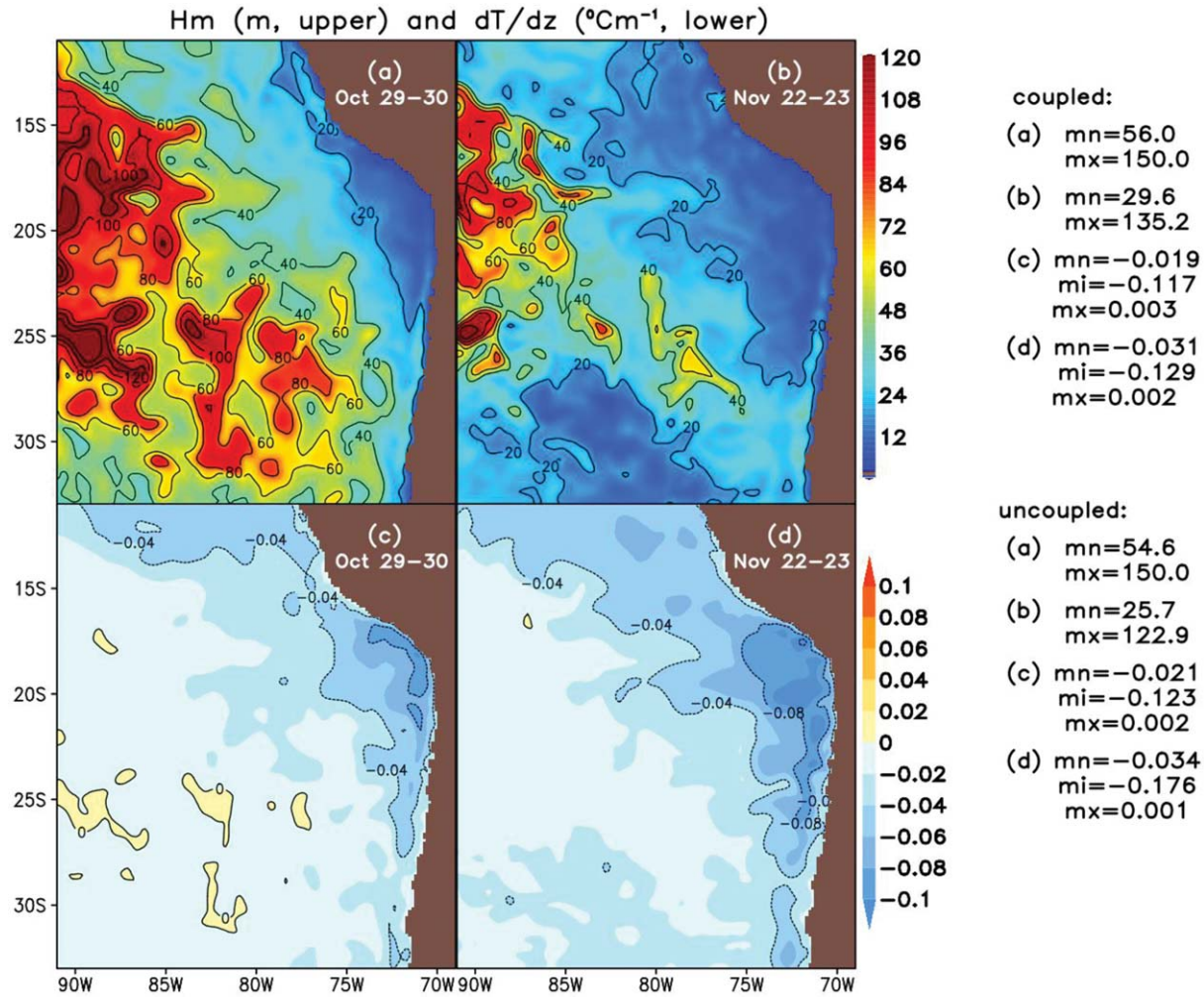

Figure 9. Coupled simulation of (top) mean mixed-layer depth and (bottom) vertical gradient of temperature between the surface and the base of the mixed-layer for the strong-forcing jet (left) and weak-forcing jet (right). The domain-mean (mn), domain-maximum (mx), and domain-minimum (mi) from the coupled and uncoupled simulations are shown in the right.

[39] The temperature change due to the horizontal advection is obtained by

$$\left.\frac{\partial T}{\partial t}\right|_{adv} = -u_{ek}\frac{\partial T}{\partial x} - v_{ek}\frac{\partial T}{\partial y} \tag{8}$$

[40] During the strong-forcing jet period, the Ekman velocity is directed offshore along the coast and to the southwest over the open ocean (Figure 11a). The directions are consistent with the long-term mean distribution [*Zheng et al*., 2010], indicating that the frequent occurrence of LLCJ has a significant contribution. The advective heat flux shows many small features, which are related to oceanic eddies that induce eddy-sized areas of positive and negative horizontal temperature gradient. The eddy-related feature also can be found in the results of *Renault et al*. [2012] in calculating horizontal advection. The negative advective heat flux denotes that the upwelled cold water from Ekman pumping in the coastal region is being advected westward. The large area of westward advective heat flux of the Chilean coast is consistent with the large Ekman transport in this area. It is also characterized by high eddy kinetic energy due to the strong but variable equatorward wind stress. This coastal transition zone extends from the coast to 600–800 km offshore and is characterized by mesoscale eddies and meanders [*Hormazabal et al*., 2004].

[41] During the weak-forcing jet period, the domain-mean Ekman velocity is smaller and convergent toward the center of the SEPH (Figure 11d). However, there is larger seaward Ekman velocity along the Chilean coast, which induces strong Ekman flux and SST decrease. The strong cooling due to the advection of upwelled water from the coast is mainly confined to the area from the coast to 100–200 km offshore. The advective heat flux near the coast is stronger, which also induces cooler water along the coast, during the weak-forcing jet period than during the strong-forcing jet period. This is due to a larger temperature gradient between the coastal upwelled cold water and the offshore downwelled warm water (Figures 8e and 8f).

[42] The SST cooling by horizontal advection is larger in the seaward direction than in the meridional direction

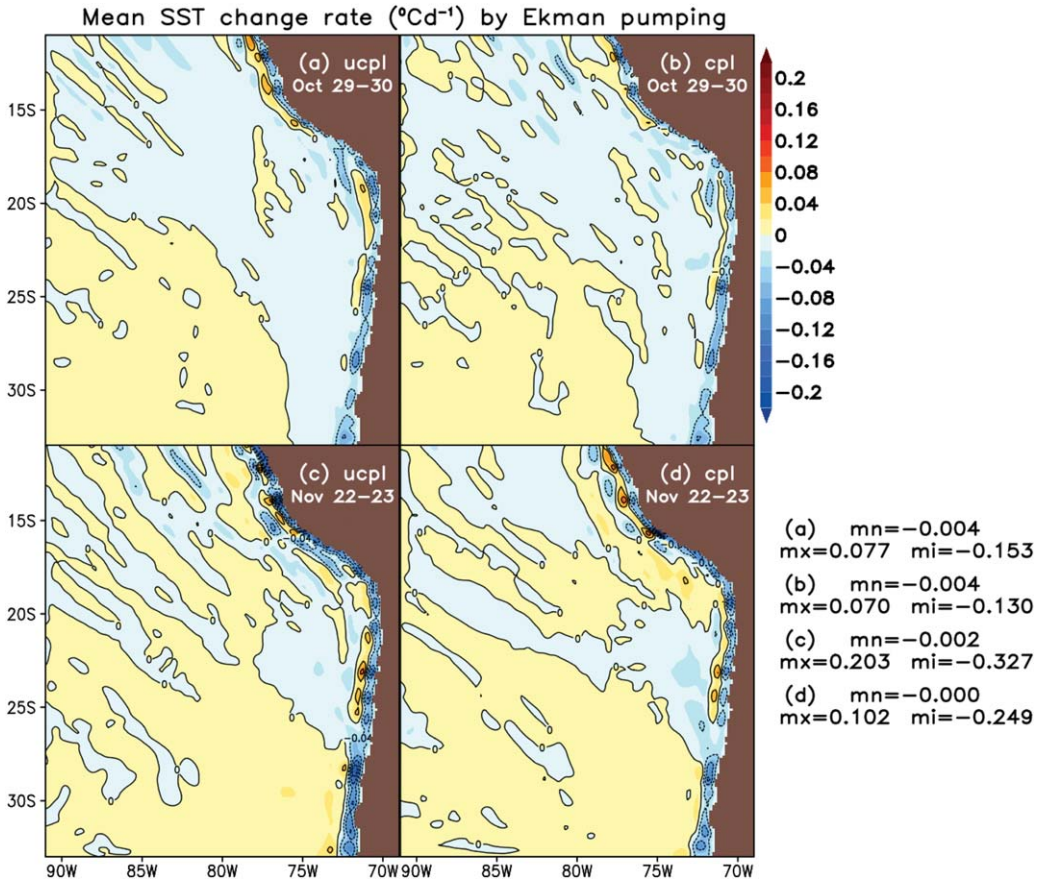

Figure 10. Temperature change rate (°C d^{-1}) due to Ekman pumping from uncoupled (left) and coupled (right) simulations (top) for strong-forcing jet from 29 to 30 October and (bottom) for weak-forcing jet from 26 to 29 November. The domain-mean (mn), domain-maximum (mx), and domain-minimum (mi) from each plot are shown in the bottom-right corner.

for both the strong-forcing and weak-forcing jet periods (figures not shown) due to the primarily westward advective heat flux by the Ekman transport (Figures11a and 11d). The area of SST cooling near the Chilean coast extends further offshore near 80°W during the strong-forcing jet period and is primarily confined within 200 km of the coast during the weak-forcing jet period. These results are consistent with the work from *Renault et al*. [2009, 2012], in which the cooling by seaward advection is more significant from 80°W to the coast for the case where the jet has a similar duration and position as the strong jet case here.

[43] The uncoupled simulation gives larger maximum cooling by horizontal advection than the coupled simulation for both the strong-forcing and weak-forcing jet periods. However, the domain mean of SST change shows more cooling from the coupled simulation than from the uncoupled simulation. This is because the uncoupled simulation also provides larger warming adjacent to the cooling cells, which cancels out the cooling rate for the domain mean. More noticeable cooling differences between uncoupled and coupled simulations are during the weak-forcing jet period, in which the horizontal advection from the uncoupled simulation transports colder water offshore due to a larger horizontal gradient off the central Chilean coast.

5.3. Impact of Vertical Entrainment

[44] SST change due to vertical entrainment is defined as the effect of the mixed-layer deepening and the temperature difference between the mixed layer and below the base of the mixed layer [*Qu*, 2001]:

$$\left.\frac{\partial T}{\partial t}\right|_{ent} = -\frac{1}{H_m}\frac{\partial H_m}{\partial t}(T_m - T_d) \tag{9}$$

where T_m and T_d are the temperatures in the mixed layer and below the base of the mixed layer, respectively. The mixed layer deepens (shoals) with time, which will lead to entrainment (detrainment), resulting in thermocline (mixed layer) water entering the mixed layer (thermocline).

[45] Since the strong-forcing jet brings cold and dry air, enhanced evaporation causes significant latent heat loss to the atmosphere (figure not shown). This large buoyancy loss increases the density at the surface and triggers vertical entrainment to bring colder water into the mixed layer from below. The strong-forcing jet also enhances TKE and leads to a rapid deepening of the mixed layer. This is evident as shown in Figures 12a and 12b for the uncoupled and coupled simulations. The domain-mean SST change rate is negative, indicating that the entrainment occurs during the strong-forcing jet period. The coupled simulation gives slightly less cooling in response to an overall weaker wind speed than the uncoupled simulation (Figure 3).

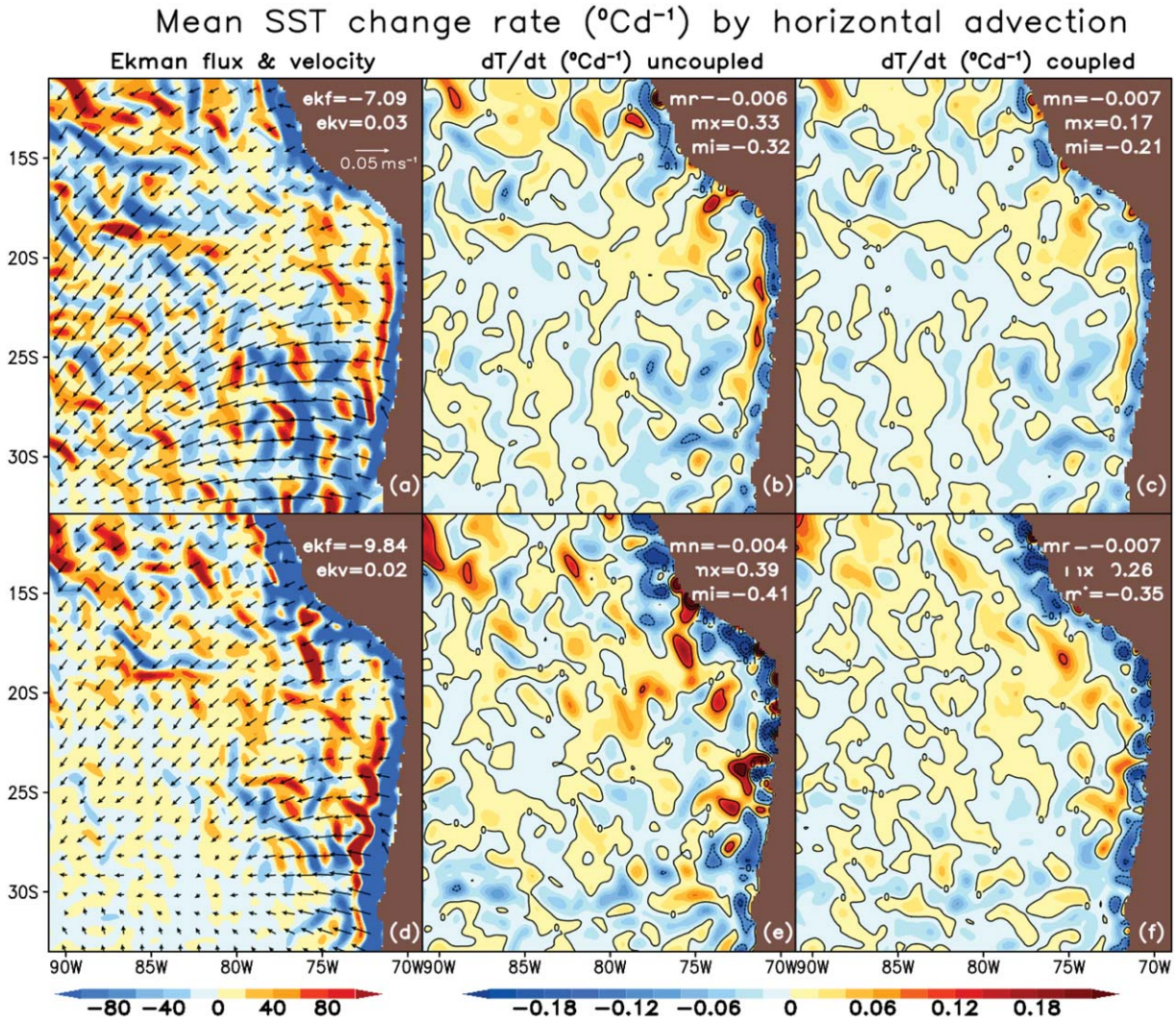

Figure 11. Coupled simulation (top) for the strong-forcing jet from 29 to 30 October and (bottom) for the weak-forcing jet from 22 to 23 November, respectively, for (a and d) Ekman advective heat flux (m^2 s^{-1}, color) and Ekman velocity (m s^{-1}, vector); for the SST change rates (°C d^{-1}) due to horizontal advection for (b and e) the uncoupled simulation and (c and f) the coupled simulation.

[46] During the weak-forcing jet period, the surface temperature increases (Figures 8d–8f), resulting in a larger vertical temperature gradient (Figure 9d). This causes more pronounced surface cooling by entrainment when the surface wind increases along the jet path (as shown in Figures 12c and 12d). The relatively stronger cooling by entrainment in *Renault et al*. [2012] may also be due to the effect of large vertical temperature gradients in the precondition before the jet event. Under the SEPH center, the mixed-layer depth shoals rapidly (Figure 9b) due to weakening of TKE, which is unable to overcome the buoyancy forcing in order to maintain the deep mixed layer. The shoaling in this area induces warm water temperature with SST change rates exceeding 0.180°C d^{-1} and 0.177°C d^{-1} for the coupled and uncoupled simulations.

5.4. Impact of Heat Fluxes

[47] The net heat flux (Q_{net}) at the ocean surface is the sum of the shortwave (solar) radiation (Q_{sw}), longwave radiation (Q_{lw}), and sensible (Q_{sh}) and latent (Q_{lh}) heat flux:

$$Q_{net} = Q_{sw} + Q_{lw} + Q_{sh} + Q_{lh} \tag{10}$$

[48] The solar and longwave radiation in the model include the effect of cloud fractional coverage determined by the predicted convective and grid-scale cloud condensate and the relative humidity. The latent and sensible heat fluxes in the model are parameterized using standard bulk aerodynamic formulas [*Fairall et al*., 2003] with the modified stability function by *Louis* [1979]. A positive heat flux anomaly indicates that the ocean surface is receiving heat, which will contribute to a positive SST anomaly.

[49] The solar radiation at the surface (Q_r), since it decreases exponentially with depth due to rapid absorption within the water column, is modified by solar extinction:

$$Q_{sw} = Q_r H_m \frac{\partial \gamma}{\partial z} \tag{11}$$

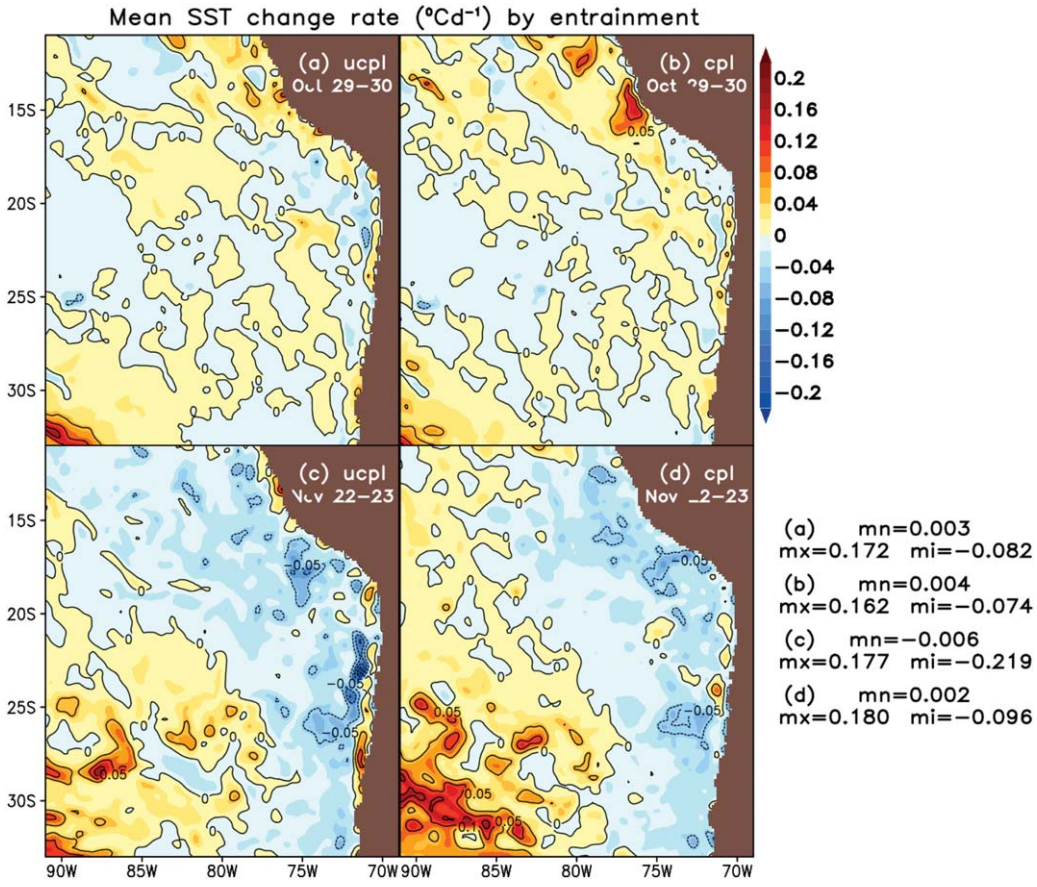

Figure 12. Mean SST change rate (°C d^{-1}) by entrainment from the uncoupled (left) and coupled (right) simulations for (a and b) strong-forcing jet from 29 to 30 October and (c and d) weak-forcing jet from 22 to 23 November.

where γ is a function describing the solar extinction. The solar extinction function uses a single Jerlov extinction profile for the entire domain and is also based on the various Jerlov water types [*Martin*, 2000]. The rate of temperature change at the surface due to the heat fluxes can be expressed as:

$$\frac{\partial T}{\partial t}\Big|_Q = -\frac{Q}{\rho_w C_{pw} H_m}, \tag{12}$$

where Q represents the heat flux terms in equation (10).

[50] There is a region of maximum warming by solar radiation along the Peruvian coast (Figure 13a) due to near-clear-sky conditions (Figure 7a) and a positive heat anomaly (figure not shown). Along the jet path, the warming is significantly reduced due to the cloud cover (Figure 7a). The near-clear-sky condition along the Peruvian coast also reduces the downward longwave heat flux (Figure 13b). At the curvature between Chile and Peru, there is a maximum heat loss by latent heat flux due to the precondition of warmer SST (Figure 8c). Compared to the SST change by the longwave radiation and sensible heat flux (which is negligible, Figure 13d), the SST change by the latent heat flux is most comparable in magnitude with the heat gain from the solar radiation (Figure 13c). The domain mean of the SST change for the solar and longwave radiation, and latent and sensible heat fluxes are 0.107, −0.024, −0.064, and −0.009°C d^{-1}, respectively. The warming by solar radiation along the Peruvian coast is reduced through the compensation of cooling from longwave radiation and latent heat flux (Figure 13e). Along the jet path, the net SST change is negative, meaning the cooling is dominated by the air-sea latent heat exchange due to the cold and dry air transported over the warmer ocean surface.

[51] During the weak-forcing jet period, cloud coverage is reduced significantly (Figure 7f), resulting in strong warming by solar radiation (Figure 14a). The domain mean SST change is 0.204°C d^{-1}, which is 90% more than during the strong-forcing jet period. More near-clear-sky coverage also reduces downward longwave heat flux (Figure 14b). During this time period, the preconditioning SST is about 1–1.5°C warmer than during the strong-forcing jet period, resulting in more heat loss by latent heat flux (Figure 14c). The distributions of SST change from the solar and longwave radiation and latent heat flux are all similar to the cloud coverage shown in Figure 7f. Strong cooling along the South Peru and north Chile coast is due to stronger wind and shallower mixed-layer depth (figure not shown). The combined SST change from all heat fluxes (Figure 14e) shows that warming from solar radiation is dominant, with only slight cooling in some locations, resulting in a domain mean warming of 0.027°C d^{-1}.

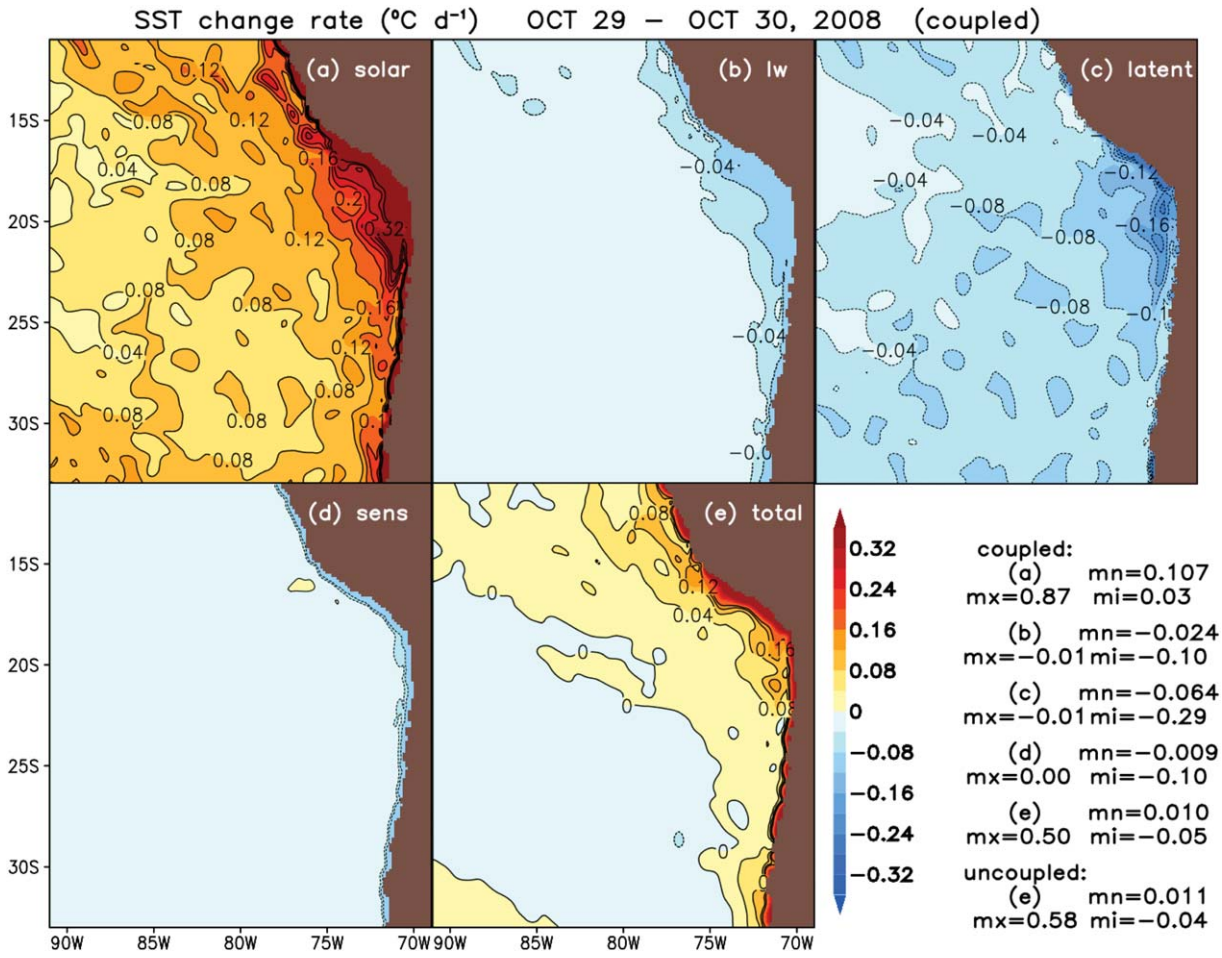

Figure 13. Temperature change rates (°C d^{-1}) from the coupled simulation by (a) shortwave radiation, (b) longwave radiation, (c) latent heat flux, (d) sensible heat flux, and (e) net heat flux for the strong-forcing jet period from 29 to 30 October 2008. The domain-mean, domain-maximum, and domain -minimum SST changes from each plot and from the uncoupled simulation by net heat flux are listed in the bottom-right corner.

[52] The uncoupled simulation provides less cooling than the coupled simulation (-0.04°C d^{-1} versus -0.05°Cd^{-1}) during the strong-forcing jet period, which is consistent with the less cloud coverage (Figures 7b and 7c). There is also more warming from the uncoupled simulation (0.20°C d^{-1} versus 0.18°C d^{-1}) during the weak-forcing period. The larger bias resulting from significantly less cloud coverage in the uncoupled simulation has induced more warming than the coupled simulation.

[53] The SST change by heat fluxes during the strong-forcing jet period is similar to the case shown in *Renault et al*. [2012], which linked the SST change to more cloud coverage and resulted in an overall cooling effect. However, for the weak-forcing jet period, the cloud coverage is significantly reduced, which resulted in an overall warming for the most of the SEP area.

5.5. Comparison of SST Changes

[54] The total mean temperature changes from the combined effect of Ekman pumping, horizontal advection, vertical entrainment, and the net heat flux associated with the coastal jet are given for the strong-forcing jet period (Figure 15) and weak-forcing jet period (Figure 16). The top figures show the SST change from the uncoupled and coupled model simulations and the bottom figures calculated from equations (1), (8), (9), and (12). The patterns of the SST change between model simulations and heat budget calculation are remarkably similar for both strong-forcing and weak-forcing periods.

[55] During the strong-forcing jet period, large cooling occurs along the coast and along the jet path and warming occurs adjacent to the jet path (Figure 15). The uncoupled simulation shows more cooling than the coupled simulation for both model simulation (Figures 15a versus 15b) and heat budget calculation (Figures 15c versus 15d). The differences of maximum SST cooling between uncoupled and coupled are $-(0.682-0.5)=-0.182$°C from the model simulation and $-(0.693-0.542)=-0.151$°C from the heat budget. These differences are due to stronger wind (Figure 3) and larger heat flux anomaly (figure not shown) in the uncoupled simulation as discussed above.

[56] During the weak-forcing jet period, more warming occurs over the open ocean under the center of the SEPH system where large subsidence is located. Despite the

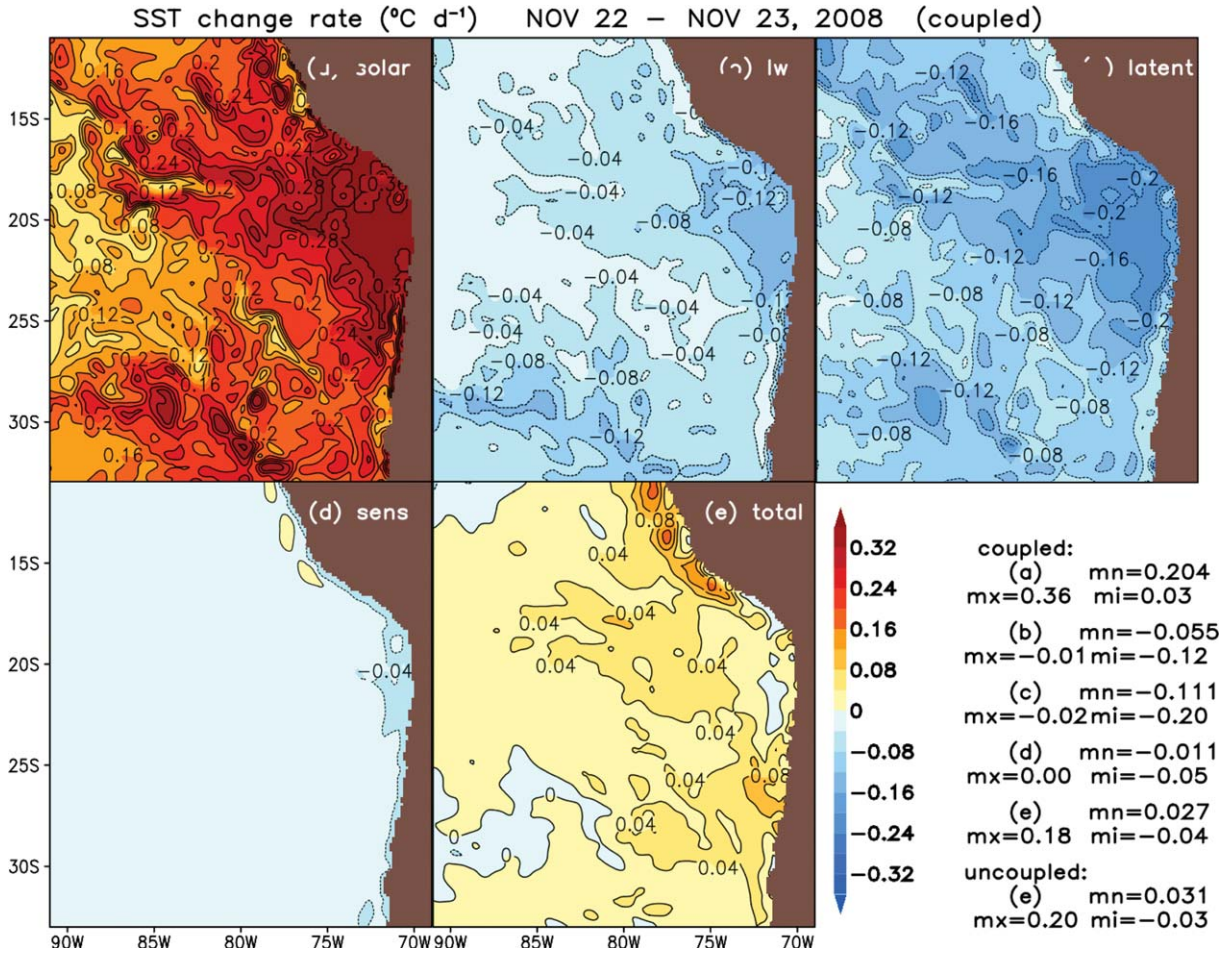

Figure 14. Same as Figure 13 except for the weak-forcing period from 22 to 23 November 2008.

overall warming in most of the domain, cooling occurs near the coastal areas. The maximum cooling during the weak-forcing jet period is in general larger than during the strong-forcing jet period, differences ranging from 0.017°C to 0.259°C (Figures 15 and 16). The uncoupled cooling (Figures 16a and 16c) is also larger than coupled (Figures 16b and 16d) for similar reasons as discussed above for the strong-forcing jet period.

[57] To further identify the different roles played by various processes for the coastal area and along the jet path for these two regimes, additional SST change rates are computed to identify the jet influence. For the coastal area, values along the coast from south to north (indicated by "O" marks in Figure 1b) are used to compute SST change rates (Figures 17a and 17b). In the coastal area, the total rates of SST change show overall cooling for both the strong-forcing and weak-forcing jet periods, with mean values of -0.045 and -0.106°C d^{-1}, respectively. The main contributions to the cooling along the coast are Ekman pumping and horizontal advection. The mean net heat flux and entrainment are positive but do not compensate for the cooling. During the strong-forcing jet period, the Ekman pumping and horizontal advection contribute 96% and 116% to the SST cooling but they are balanced by net heat flux and entrainment, in which net heat flux provides −88% for the warming, 64% more warming than the entrainment. The uncoupled simulation shows more net cooling along the coast during the strong jet period, mainly due to the horizontal advection by offshore transportation of the upwelled cold water. These features for the different process along the coast are also reflected in SST change during the weak-forcing period.

[58] Results from *Renault et al*. [2012] indicate that although Ekman pumping is important in the coastal area, entrainment is the most significant contribution to the coastal cooling. This differs from this study in which entrainment has a relatively small contribution. One possible reason may be differences in vertical resolution (41 levels versus 32 levels in *Renault et al*. [2012]). Another important factor is differences in preconditioning of the mixed layer depth for two events. Both the factors can contribute to different vertical temperature gradients, resulting in different entrainment rate. As examined in the study of *Renault et al*. [2012], the error in representation of the wind dropoff can also generate inaccuracies in coastal upwelling and Ekman pumping.

[59] The SST changes computed along the jet path (Figures 17c and 17d) use model values at locations marked with "P" in Figure 1b, starting from the southeast corner, northward then southward until reaching the southwest corner of the jet path grid. The jet path is thus defined differently for the strong-forcing and weak-forcing jets

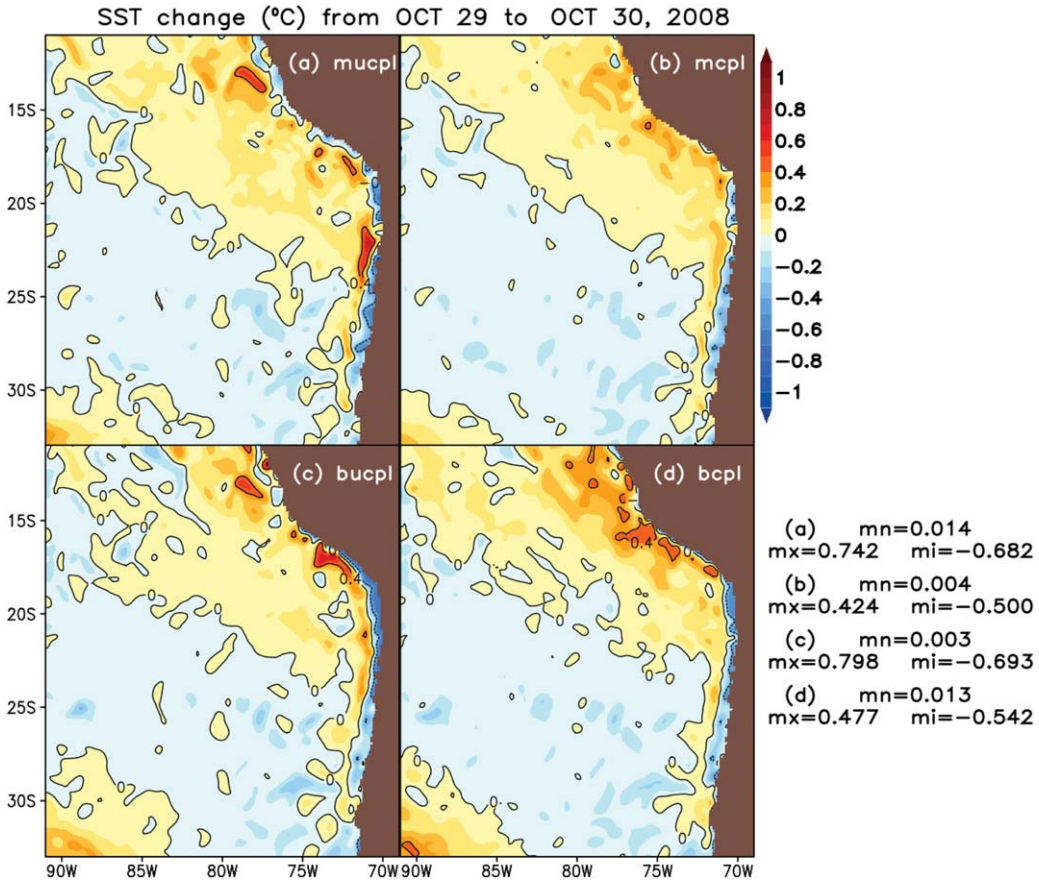

Figure 15. SST changes for the strong-forcing jet period from 29 to 30 October 2008 for the uncoupled (left) and coupled (right) for (a and b) model simulations; and (c and d) total heat balance calculated from equations (1), (8), (9), and (12).

according to their respective features. As shown in Figure 1b, the "P" marks (both red and green) are for the strong-forcing jet and green "P" marks only are for the weak-forcing jet. In contrast to the coastal area discussed above, the SST change rate caused by the Ekman pumping and horizontal advection is small or negligible from both the coupled and uncoupled simulations, especially for the strong-forcing jet period. The net heat flux plays a major role along the jet path for both the strong-forcing and weak-forcing jet periods. For the strong-forcing jet period, the net heat loss, largely due to latent heat flux (Figure 13), causes cooling of 68% (coupled) to 65% (uncoupled) of the overall cooling along the jet path (Figure 17c). A smaller portion (28% from coupled and 30% from uncoupled) of the cooling results from horizontal advection. For the weak-forcing jet period, the net heat flux is positive (Figure 14e), resulting in substantial warming [0.041°C d^{-1} (coupled) to 0.045°C d^{-1} (uncoupled)]. The warmings, however, are significantly compensated by entrainment, which induced cooling up to −0.019°C d^{-1} from both the coupled (Figure 12d) and uncoupled (Figure 12c) simulations.

[60] The area along the jet path in the present study completely covers the jet within the domain; therefore, it is much larger than the offshore box in *Renault et al*. [2012], which only include offshore 30–150 km. The current setting for the jet path enables us to investigate air-sea interaction directly under the jet influence. In contrast to the result that air-ocean net heat flux exchange is the most prominent process in cooling the SST, *Renault et al*. [2012] has indicated that vertical mixing plays a primary role in the offshore area as well as along the coast. This may be attributed to a few factors including the model configuration, boundary conditions, preconditioning for different events, and the different definitions for the jet path and offshore box.

6. Discussion and Summary

[61] Based on the location of the SEPH center relative to the central Chilean coastline, the LLCJ is characterized as either a strong-forcing jet or weak-forcing jet [*Jiang et al*., 2010]. The study of the LLCJ indicated that there are significantly different characteristics and dynamics between the strong-forcing and weak-forcing jets [*Jiang et al*., 2010]. As the SST change associated with the weak-forcing jet period has not been investigated before, and the use of a two-way fully coupled air-ocean model was lacking in the previous study [*Renault et al*. 2012], we have conducted our study for both the strong-forcing jet period and weak-forcing jet period during the VOCALS field campaign from 20 October to 30 November 2008 using results from uncoupled and coupled COAMPS simulations.

[62] Model results from the uncoupled and coupled simulations are validated with satellite-observed wind,

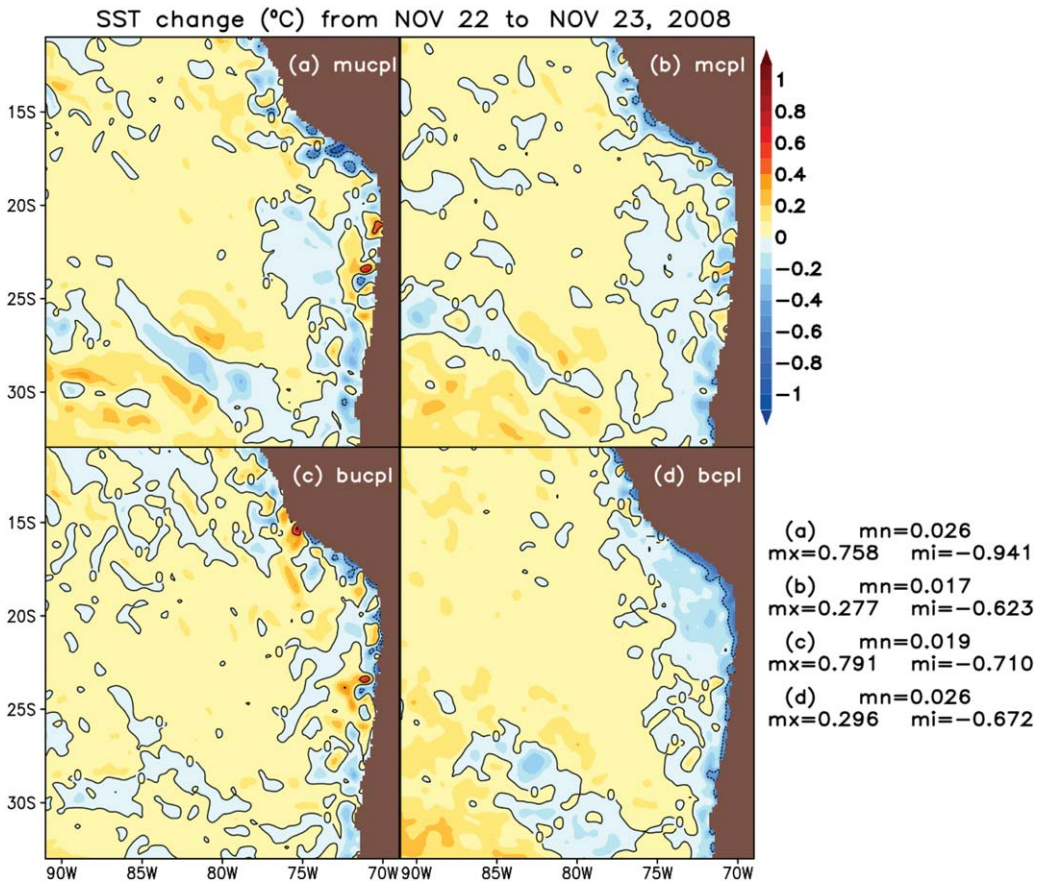

Figure 16. Same as Figure 15 except for the weak-forcing jet period from 22 to 23 November.

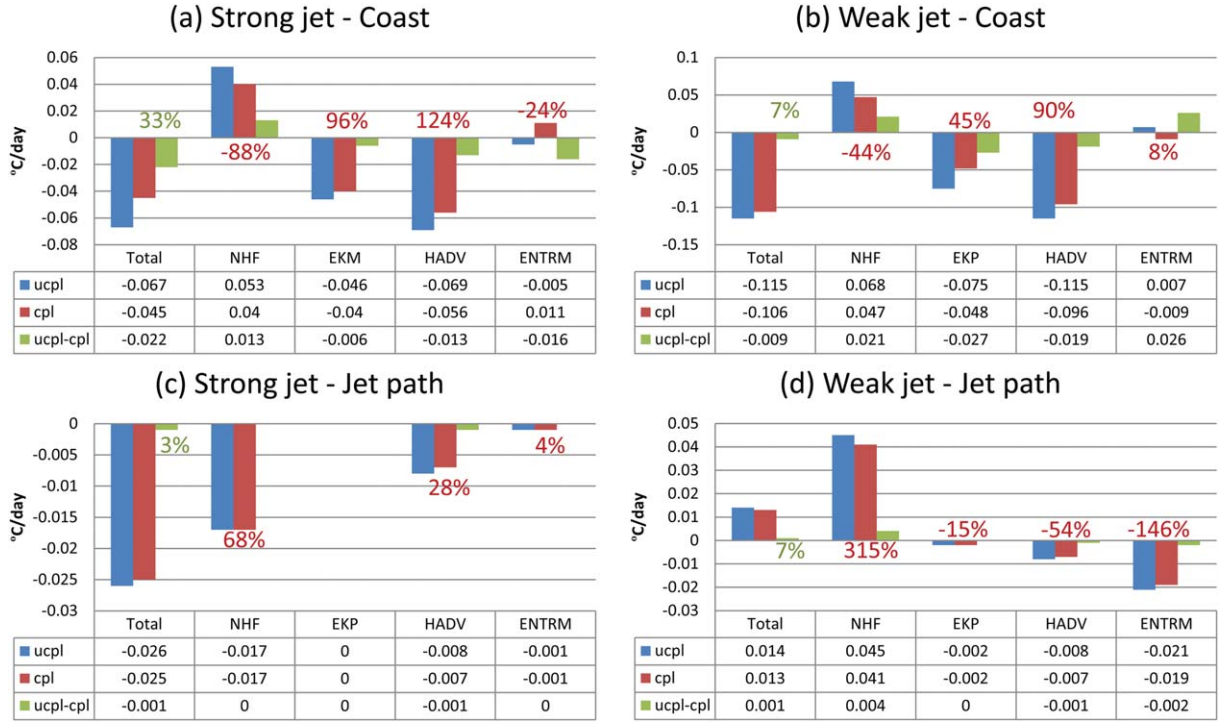

Figure 17. The SST change rates (°C d^{-1}) for (a and b) the coastal areas and (c and d) along the jet path. Figures 17a and 17c are for the strong-forcing jet period and Figures 17b and 17d are for the weak-forcing jet period. The point locations for the coastal and jet path are shown in Figure 1.

temperature, and CLWP for a strong-forcing jet case from 29 to 30 Octoberand a weak-forcing jet case from 22 to 23 November 2008. Results compare the different characteristics in the MBL and the SST responses between the strong-forcing and weak-forcing jets. The area of mean wind speed greater than 8 ms^{-1} for the strong-forcing jet case is seven times larger than the area for the weak-forcing jet. Colder and drier air is carried by the strong-forcing jet with about 80% of the domain covered by CLPW greater than 60 g m^{-2}. The SST is generally reduced with colder water extending further offshore from the Chilean coast. In contrast, the weak-forcing jet has mean positive anomalies for both the air temperature and water vapor, resulting in warmer and moister air properties. Only about 40% of the domain is covered by clouds, which is consistent with warmer SST over most of the domain and reduced cold water coverage near the coast.

[63] Overall, statistical results indicate that the two-way coupled simulation is generally more skillful than the uncoupled simulation, with smaller overall absolute bias. The coupled overall absolute bias is 50% less for the surface wind speed, 70% less for the CLWP, and 15% less for SST, as compared to the uncoupled simulation. Subsequently, we expect that the estimation of each process for the SST change from the coupled simulation is closer to observed than the uncoupled simulation. The coupled simulation is able to adjust SST cooling from the uncoupled simulation, most significantly during the strong-forcing jet period along the coastal area mainly due to offshore transport of upwelled cold water. The coupled simulation also significantly reduces the excess warming from the uncoupled simulation by providing better cloud coverage.

[64] Four major processes, Ekman pumping, horizontal advection, vertical entrainment, and net surface heat flux exchange, are analyzed to determine their relative contributions to the SST change with the confidence of wind dropoff representation from the model. The SST changes during the strong-forcing and weak-forcing jet periods are remarkably consistent considering the estimation from four processes and the model simulation. The total effect of Ekman pumping, horizontal advection, entrainment, and the net heat flux on the SST results in an overall cooling along the coast and the jet path during the strong-forcing jet period. The feature differs for the weak-forcing jet period, which the cooling is only restricted along the coastal area and warming is along the jet path and offshore area.

[65] The importance of each process on the modulation of the SST differs between the coastal and open ocean areas. Strong upwelling due to the divergence of the Ekman transport associated with negative wind stress curl and horizontal advection are the most prominent processes in cooling the SST along the coast during both the strong-forcing and weak-forcing jet periods. This differs from the results of *Renault et al*. [2012], which indicate that entrainment and Ekman pumping are the primary and secondary contributors to coastal cooling, respectively. The reason may be due to different vertical resolution and the preconditioning for the mixed layer depth in *Renault et al*. [2012]. Both factors can contribute to different vertical temperature gradients that can induce rather dissimilar entrainment heat. The bias of wind dropoff due to poorly resolved coastal zone of TMI SST can also generate inaccuracies in Ekman pumping and coastal upwelling in *Renault et al*. [2012].

[66] Along the jet path, the effects of Ekman pumping and entrainment on the SST change are negligible during the strong-forcing jet period. The most prominent process is air-sea heat exchange in cooling the SST with more than 68% contribution. There is a smaller contribution (28%) from the horizontal advection during the strong jet period. This differs from the results of *Renault et al*. [2012], which indicates that the vertical mixing plays a primary role in the offshore box. This may be attributed to model configuration, boundary conditions, preconditioning for different events, and the different definitions for the jet path and offshore box. During the weak-forcing jet period, air-sea heat exchange is also important, but with a net warming effect. Although the entrainment induces significant cooling, it is not able to compensate for the strong warming due to less cloud coverage.

[67] The coupled simulation may mitigate weaknesses in the uncoupled simulation due to inappropriate representation of the atmospheric bottom boundary condition along coastal areas, such as the TMI SST used to force the atmospheric simulation [*Renault et al*., 2012]. The poorly resolved coastal zone in TMI SST cannot accurately resolve the wind dropoff due to its physical forcing. Uncoupled simulations in *Renault et al*. [2012] also show bias in the estimation of turbulent heat fluxes since the atmospheric stability conditions are associated with the air-sea temperature difference, which can be better provided from the coupled simulation as shown in the present study. Uncoupled atmospheric simulations in *Renault et al*. [2012] show weaknesses in representing low clouds, which in turn may also lead to biases of surface heat fluxes. The comparison of CLWP in the present study has shown that the coupled simulation provides 70% less overall absolute bias than the uncoupled simulation.

[68] **Acknowledgments.** We would like to thank the reviewers for their constructive and many helpful suggestions for improving this paper. This research is supported by the NRL Base Program, PE 0602435N. Computations were performed on the IBM P4+ at the Naval Oceanographic Office (NAVO) Major Shared Resource Center (MSRC) at Stennis Space Center, Mississippi.

References

Albert, A., V. Echevin, M. Lévy, and O. Aumont (2010), Impact of nearshore wind stress curl on coastal circulation and primary productivity in the Peru upwelling system, *J. Geophys. Res.*, *115*, C12033, doi:10.1029/2010JC006569.

Allard, R. A., T. J. Campbell, T.A. Smith, T.G. Jensen, J.A. Cummings, S. Chen, J. Doyle, X. Hong, R.J. Small, and S. N. Carroll (2010), Validation test report for the coupled ocean/atmosphere mesoscale prediction system (COAMPS) version 5.0, NRL/MR/7320-10-9283, p. 160. Naval Research Laboratory, Stennis Space Center., MS 39529-5004. September 27, 2010.

Capet, X. J., P. Marchesiello, and J. C. McWilliams (2004), Upwelling response to coastal wind profiles, *Geophys. Res. Lett.*, *31*, L13311, doi:10.1029/2004GL020123.

Chen, S., T. J. Campbell, H. Jin, S. Gaberŝek, R. M. Hodur, and P. Martin (2010), Effect of two-way air-sea coupling in high and low wind speed regimes, *Mon. Weather Rev.*, *138*, 3579–3602.

Clement, A. C., R. Burgman, and J. R. Norris (2009), Observational and model evidence for positive low level cloud feedback, *Science*, *325*, 460–464. doi:10.1126/science.1171255.

Cummings, J. (2005), Operational multivariate ocean data assimilation, *Q. J. R. Meteorol. Soc.*, *131*, 3583–3604.

Dewitte, B., M. Ramos, V. Echevin, O. Pizarro, and Y. duPenhoat (2008), Vertical structure variability in a seasonal simulation of a medium-resolution regional model simulation of the south eastern Pacific, *Prog. Oceanogr.*, *79*, 120–137.

Edwards, K. A., A. M. Rogerson, C. D. Winant, and D. P. Rogers (2001), Adjustment of the marine atmospheric boundary layer to a coastal cape, *J. Atmos. Sci.*, *58*, 1511–1528, doi:10.1175/1520-0469(2001)058<1511:AOTMAB>2.0.CO;2.

Fairall, C., E. Bradley, J. Hare, A. Grachev, and J. Edson (2003), Bulk parameterization of air-sea fluxes: Updates and Verification for the COARE Algorithm, *J. Clim.*, *16*, 571–591.

Garreaud, R., and R. Muñoz (2005), The low-level jet off the subtropical west coast of South America: Structure and variability, *Mon. Weather Rev.*, *133*, 2246–2261, doi:10.1175/MWR2972.1.

Gill, A. E. (1982), *Atmosphere-Ocean Dynamics*, Academic, San Diego, Calif.

Halpern, D. (2002), Offshore Ekman transport and Ekman pumping off Peru during the 1997–1998 El Niño, *Geophys. Res. Lett.*, *29*(5), 1075, doi:10.1029/2001GL014097.

Harshvardhan, R. Davis, D. A. Randall, and T. G. Corsetti (1987), A fast radiation parameterization for general circulation models, *J. Geophys. Res.*, *92*, 1009–1016.

Hodur, R. M. (1997), The Naval Research Laboratory's Coupled Ocean/Atmospheric Mesoscale Prediction System (COAMPS), *Mon. Weather Rev.*, *125*, 1414–1430.

Hodur, R. M., X. Hong, D. J. Doyle, J. Pullen, J. Cummings, P. Martin, and M. A. Rennic (2002), The Coupled Ocean/Atmosphere Mesoscale Prediction System (COAMPS), *Oceanography*, *15*(1), 88−98.

Hong, X., P. J. Martin, S. Wang, and C. Rowley (2009a), High SST variability south of Martha's Vineyard: Observation and modeling study, *J. Mar. Syst.*, *78*, 59–76.

Hong, X., J. A. Cummings, P. J. Martin, and J. Doyle (2009b), Ocean data assimilation: A coastal application, in *Data Assimilation for Atmospheric, Oceanic and Hydrologic Applications*, edited by S. K. Park and L. Xu, pp. 269–292, Springer, Berlin.

Hormazabal, S., G. Shaffer, and O. Leth (2004), Coastal transition zone off Chile, *J. Geophys. Res.*, *109*, C01021, doi:10.1029/2003JC001956.

Jiang, Q., S. Wang, and L. O'Neill (2010), Some insights into the characteristics and dynamics of the Chilean low-level coastal jet, *Mon. Weather Rev.*, *138*, 3185–3206.

Jin, X., C. Dong, J. Kurian, J. C. McWilliams, D. Chelton, and Z. Li (2009), SST-wind interaction in coastal upwelling: Oceanic simulation with empirical coupling, *J. Phys. Oceanogr.*, *39*, 2957–2970, doi:10.1175/2009JPO4205.1.

Kain, J. S., and M. Fritsch (1990), A one-dimensional entraining/detraining plume model and its application in convective parameterization, *J. Atmos. Sci.*, *47*, 2784–2802.

Louis, J.-F. (1979), A parametric model of vertical eddy fluxes in the atmosphere, *Boundary Layer Meteorol.*, *17*, 187–202.

Louis, J. F., M. Tiedtke, and J. F. Geleyn (1982), *A short history of the operational PBL-parameterization of ECMWF, in Proceedings of the 1981 ECMWF Workshop on Planetary Boundary Layer Parameterization*, pp. 59–79, Eur. Cent. for Medium Range Weather Forecasts, Shinfield Park, Reading, Berkshire.

Martin, P. J. (2000), Description of the NAVY Coastal Ocean Model Version 1.0, NRL Rep.: NRL/FR/7322-00-9962, Naval Research Laboratory, Stennis Space Center, MS 39529–5004, December 31, 2000.

Mellor, G. L., and T. Yamada (1982), Development of a turbulence closure for geophysical fluid problems, *Rev. Geophys. Space Phys.*, *20*, 851–875.

Muñoz, R., and R. Garreaud (2005), Dynamics of the low-level jet off the subtropical west coast of South America, *Mon. Weather Rev.*, *133*, 3661–3677, doi:10.1175/MWR3074.1.

Qu, T. (2001), Role of ocean dynamics in determining the mean seasonal cycle of the South China Sea surface temperature, *J. Geophys. Res.*, *106*(C4), 6943–6955.

Pickett, M. H., and J. D. Paduan (2003), Ekman transport and pumping in the California Current based on the U.S. Navy's high-resolution atmospheric model (COAMPS), *J. Geophys. Res.*, *108*(C10), 3327, doi:10.1029/2003JC001902.

Pizarro, O., A. J. Clarke, and S. Van Gorder (2001), El Niño sea level and currents along the South American coast: Comparison of observations with theory, *J. Phys. Oceanogr.*, *31*, 1891–1903, doi:10.1175/1520-485(2001)031.

Pizarro, O., G. Shaffer, B. Dewitte, and M. Ramos (2002), Dynamics of seasonal and interannual variability of the Peru-Chile Undercurrent, *Geophys. Res. Lett.*, *29*(12), 1581, doi:10.1029/2002GL014790.

Rahn, D. A., and R. Garreaud (2010), Marine boundary layer over the subtropical southeast Pacific during VOCALS-REx—Part 1: Mean structure and diurnal cycle, *Atmos. Chem. Phys.*, *10*, 4491–4506.

Renault, L., B. Dewitte, M. Falvey, R. Garreaud, V. Echevin, and F. Bonjean (2009), Impact of atmospheric coastal jet off central Chile on sea surface temperature from satellite observations (2000–2007), *J. Geophys. Res.*, *114*, C08006, doi:10.1029/2008JC005083.

Renault, L., B. Dewitte, P. Marchesiello, S. Illig, V. Echevin, G. Cambon, M. Ramos, O. Astudillo, P. Minnis, and J. K. Ayers (2012), Upwelling response to atmospheric coastal jets off central Chile: A modeling study of the October 2000 event, *J. Geophys. Res.*, *117*, C02030, doi:19.1029/2011JC007446.

Ruggles, K.W., 1970. The vertical mean wind profile over the ocean in light to moderate winds. *Jr. Application Meleorology 9*, 389–395.

Rutledge, S. A. and P. V. Hobbs (1983), The mesoscale and microscale structure of organization of clouds and precipitation in midlatitude cyclones. VIII: A model for the ''seeder-feeder'' process in warm-frontal rainbands, *J. Atmos. Sci.*, *40*, 1185–1206.

Soto-Mardones, L., A. Parés-Sierrac, and R. Duraz (2004), Ekman modulation of the sea-surface temperature on the Eastern South Pacific, *Deep Sea Res., Part II*, *51*, 551–561.

Thomson, R. E. and I. V. Fine (2003), Estimating mixed layer depth from oceanic profile data, *J. Atmos. Oceanic Technol.*, *20*, 319–329.

Wang, S., Q. Wang, and J. Doyle (2002), Some improvement of Louis surface flux parameterization, in *15th Symp. on Boundary Layers and Turbulence, Preprints*, pp. 547–550, Am. Meteor. Soc., Wageningen, Netherlands.

Wang, S., L. W. O'Neill, Q. Jiang, S. P. de Szoeke, X. Hong, H. Jin, W. T. Thompson, and X. Zheng (2011), A regional real-time forecast of marine boundary layers during VOCALS-Rex, *Atmos. Chem. Phys.*, *11*, 421–437.

Wood, R., and D. L. Hartmann (2006), Spatial variability of liquid water path in marine low clouds: The importance of mesoscale cellular convection, *J. Clim.*, *19*, 1748–1764.

Wood, R., and the VOCALS Scientific Working Group (2010), VOCALS-Regional Experiment (VOCALS-REx), Experimental design overview. [Available at http://www.eol.ucar.edu/projects/vocals/science_planning/VOCALS_EDO_Final.pdf.].

Wyant, M. C., C. S. Bretherton, H. A. Rand, and D. E. Stevens (1997), Numerical simulations and a conceptual model of the stratocumulus to trade cumulus transition, *J. Atmos. Sci.*, *54*, 169–192.

Yang, J. (2006), The seasonal variability of the Arctic ocean Ekman transport and its role in the mixed layer heat and salt fluxes, *J. Clim.*, *19*, 5366–5387.

Zheng, Y., T. Shinoda, G. N. Kiladis, J. Lin, E. J. Metzger, H. E. Hurlburt, and B. S. Giese (2010), Upper-ocean processes under the stratus cloud deck in the Southeast Pacific Ocean, *J. Phys. Oceanogr.*, *40*, 103–120.